The Value of Dynamic Downscaling a CMIP6 Global Climate Model Simulation over the Floridan Aquifer

VASUBANDHU MISRA[a,b] AND C. B. JAYASANKAR[b]

[a] *Department of Earth, Ocean and Atmospheric Science, Florida State University, Tallahassee, Florida*
[b] *Center for Ocean-Atmospheric Prediction Studies, Florida State University, Tallahassee, Florida*

(Manuscript received 10 March 2025, in final form 7 July 2025, accepted 18 August 2025)

ABSTRACT: The Floridan Aquifer (FA), a source of freshwater to a large population in the southeastern United States, is now threatened by depletion for a variety of reasons including climate variations and change. The hydroclimate variations in the region are dictated by high frequency variations including diurnal variability and extremes of precipitation. A regional coupled ocean–atmosphere model (RCM) at 10-km grid spacing centered over the FA is used to downscale over a 30-yr period (1985–2014). The Community Earth System Model, version 2 (CESM2), historical simulation, which is part of the Coupled Model Intercomparison Project phase 6 (CMIP6), is used as the lateral boundary forcing for the RCM. The RCM simulates several mesoscale features in the domain that are verified with observations including tropical cyclones, extreme rainfall events, the daily rainfall distribution over the summer (wet) season, the daily variability of surface temperature, the diurnal variability of precipitation, and the variations in the Loop Current in the neighboring oceans. Additionally, the RCM demonstrates improvements in reducing the seasonal bias of some of the surface variables in the RCM simulation compared to the corresponding CESM2 integration. Furthermore, the RCM fills the critical gap of providing high temporal resolution data for potential climate applications that are in many instances unavailable from the global climate simulations. This study clearly demonstrates the benefits of dynamic downscaling the climate over a region like FA, which are impacted by a variety of mesoscale features both in the atmosphere and in the ocean.

SIGNIFICANCE STATEMENT: This paper presents a 30-yr, high-resolution (10 km) dynamically downscaled simulation using a regional coupled ocean–atmosphere model (RCM) centered over the Floridan Aquifer (FA), a key freshwater source for the southeastern United States. Forced by a global climate model, the simulation improves the representation of mean climate and high-frequency variability over the FA. The RCM captures fine-scale climate features such as daily and diurnal rainfall, surface temperature variability, and Gulf of Mexico Loop Current behavior—elements not well resolved in the global model. These refinements demonstrate the value of dynamic downscaling for understanding climate impacts on water resources. The findings offer a pathway for applying regional climate information in sectors such as hydrology, agriculture, and water management under current and future climate scenarios.

KEYWORDS: North America; Regional models; Climate variability; Diurnal effects; Seasonal cycle

1. Introduction

The Floridan Aquifer (FA), which lies beneath all of Florida and parts of Alabama, Georgia, and South Carolina, is one of the world's most productive aquifers, supplying drinking water to over 10 million people (Marella and Berndt 2005). In fact, it is reported that 92% of Florida's population has its drinking water withdrawn from the FA (Marella 2015). Besides its use for drinking water, the water from the FA is also extensively utilized in these states for irrigation and industrial use. Therefore, the FA is identified as a critical resource of freshwater. The surface water resources are a main source of recharge for the underlying aquifer. Hence, potential changes or variations in weather and climate patterns are likely to influence the quantity and quality of water available to recharge and replenish the water resources (Obeysekera et al. 2017).

Florida, the third most populous state in the country, boasts a population exceeding 21 million (NOAA 2013). This number is steadily growing at a rate of approximately 300 000 individuals per year, with a notable concentration in the coastal shoreline counties. In addition, half of the 67 counties in Florida border either the Gulf of Mexico or the Atlantic Ocean and 76% of Floridians reside in these coastal counties. It is evident based on the data on water withdrawal that groundwater resources play a significant role in providing approximately 63% of Florida's total water supply and 85% of its public water (Marella and Dixon 2015). Despite Florida's average annual rainfall of 137 cm (or 54 in.), the extraction of fresh groundwater is nearing unsustainable levels in many parts of the state [Florida Oceans and Coastal Council (FOCC 2010); Maliva et al. 2021]. The overpumping of the aquifer on account of over usage and demand for freshwater has resulted in the lowering of the potentiometric surface, consequently increasing the likelihood of saltwater intrusion from the deeper saline zones (Spechler 1994; Obeysekera et al. 2017). Furthermore, the low-elevation, porous karstic bedrock, extensive coastlines of

---

Supplemental information related to this paper is available at the Journals Online website: https://doi.org/10.1175/JAMC-D-25-0037.s1.

Corresponding author: Vasubandhu Misra, vmisra@fsu.edu

DOI: 10.1175/JAMC-D-25-0037.1

Florida, and upstream surface water diversions make Florida extremely vulnerable to saltwater intrusion (McVoy et al. 2012; Dessu et al. 2018; Charles et al. 2019). Therefore, there is a certain urgency to understand and mitigate some of these impacts from understanding how climate variations and change over the FA could potentially further exacerbate the freshwater resources in the state.

Several studies have indicated that Florida's climate and its variations are somewhat unique to the continental United States, given its subtropical location, peninsular geography, and surrounded by relatively warm oceans with unique bathymetry (Misra et al. 2017a,b). Florida's hydroclimate is characterized especially in the wet season (summer) by mesoscale events on the order of 10–1000 km (Maxwell et al. 2012; Prat and Nelson 2013; Misra et al. 2017b; Shi and Misra 2020), which serves as a challenge to some of contemporary coarse climate models (Obeysekera et al. 2015). The challenge for simulating or predicting climate over the region is that variations in climate over both the oceans and atmosphere are dictated by mesoscale features that require a relatively high horizontal resolution of models compared to most of the current routinely run climate models (Volosciuk et al. 2015; Hewitt et al. 2020). For instance, landfalling tropical cyclones (TCs) and convective thunderstorms associated with sea-breeze circulations are important contributors to the seasonal hydroclimate of the region. Similarly, Misra et al. (2016) show that the seasonal variations in mesoscale surface ocean currents like the Loop Current in the Gulf of Mexico play an important role in the seasonal hydroclimate of Florida. Likewise, the shallow bathymetry of the west Florida shelf also plays a critical role in regulating the seasonal hydroclimate of Florida (Misra et al. 2016). Majority of these features are not permitted, let alone resolved in most of the current global climate models that are routinely run at ~120-km horizontal grid spacing. Putrasahan et al. (2017) show that the mesoscale variations in the Loop Current system in the Gulf of Mexico is critical for the air–sea interactions, especially in the case of warm core eddies that periodically spin off the Loop Current. In such instances, the oceanic forcing of the atmospheric fluxes is apparent (Shay et al. 2000; Meunier et al. 2024). In fact, van der Ent and Savenije (2013) and Chan and Misra (2010) identify the Atlantic warm pool region of the Caribbean Sea, Gulf of Mexico, and the subtropical western Atlantic Ocean as a major source of moisture for terrestrial precipitation over southern and eastern United States.

In a comprehensive analysis of precipitation in observations, atmospheric reanalyses, climate model simulations, and statistically downscaled models over Florida, Srivastava et al. (2020) find that even reanalyses show large uncertainty, especially in the summer. Similarly, they indicate that climate models also show large uncertainty with even the seasonal cycle being misrepresented in some of the models. These issues become far more acute when precipitation extremes are examined in the models (Srivastava et al. 2022; Rahimi et al. 2024). Srivastava et al. (2022) suggest that the statistical models tend to perform better than all the dynamical models and atmospheric reanalyses because they are bias-corrected datasets. However, their performance in projecting the precipitation extremes or variability in a future warming climate could be limited (Chen and Zhang 2021). It should also be noted that many studies have recognized the limitations of purely metric-based evaluation of precipitation in model simulations as they ignore the physical processes that drive precipitation, which could throw additional light on the fidelity of the model (Alexander et al. 2020; Srivastava et al. 2022). For a region like Florida that displays significant rain-bearing systems in the mesoscale (Rickenbach et al. 2015), it becomes extremely difficult to statistically downscale from a global model that does not account for them, or the observational records are not long enough in time to resolve these features to develop robust statistics on them. This becomes more of a challenge to project for such rain events in a future changing climate from statistical downscaling effort that hinges on relationships used in the historical training period that may not necessarily sustain in the projected climate (Lanzante et al. 2018).

In this study, we present the results of the comprehensive evaluation of the first of its kind Coupled Model Intercomparison Project phase 6 (CMIP6)–forced high-resolution (10-km) regional coupled ocean–atmosphere model (RCM) integration of a 30-yr period centered over the FA, for the present-day climate of 1985–2014. The RCM integration analyzed in this study is forced by the Community Earth System Model, version 2 (CESM2; Danabasoglu et al. 2020), a state-of-the-art fully coupled global climate model. CESM2 was one of the participating models in the CMIP6 (Eyring et al. 2016). The analysis of this 30-yr downscaled data presented in the paper includes an extensive validation of both atmospheric and oceanic variables from the RCM with observations and reanalysis. Furthermore, we also compare the model simulations of the global and regional model integrations to highlight the differences and the potential value of dynamical downscaling. In the following section, the model description and its setup are detailed followed by a discussion of the verification data used in the study. The results are discussed in section 4, and conclusions are given in section 5.

2. Model description and setup

We choose to dynamically downscale the CESM2 for the domain shown in Fig. 1. The atmospheric component of CESM2 is the Community Atmosphere Model, version 6 (CAM6; Bogenschutz et al. 2018), which uses a nominal 1° horizontal resolution (1.25° longitude × 0.95° latitude) with 32 vertical levels and a model top of 3.6 hPa (~40 km). The ocean model in CESM2 is the Parallel Ocean Program, version 2 (POP2; Smith et al. 2010; Danabasoglu et al. 2012), with a nominal 1° horizontal resolution with enhanced resolution near the equator and 60 vertical levels. CESM2 also uses a Community Land Model, version 5 (CLM5; Lawrence et al. 2019), and Community Ice Code, version 5 (CICE5; Hunke et al. 2015). CESM2 represents a progression in the community-wide development of the numerical climate model and is a good representation of the current state of the art in Earth system modeling (Simpson et al. 2020). A comprehensive review of the performance of the CESM2 has been conducted in several studies, which generally conclude that its fidelity ranks within the top 10% of other

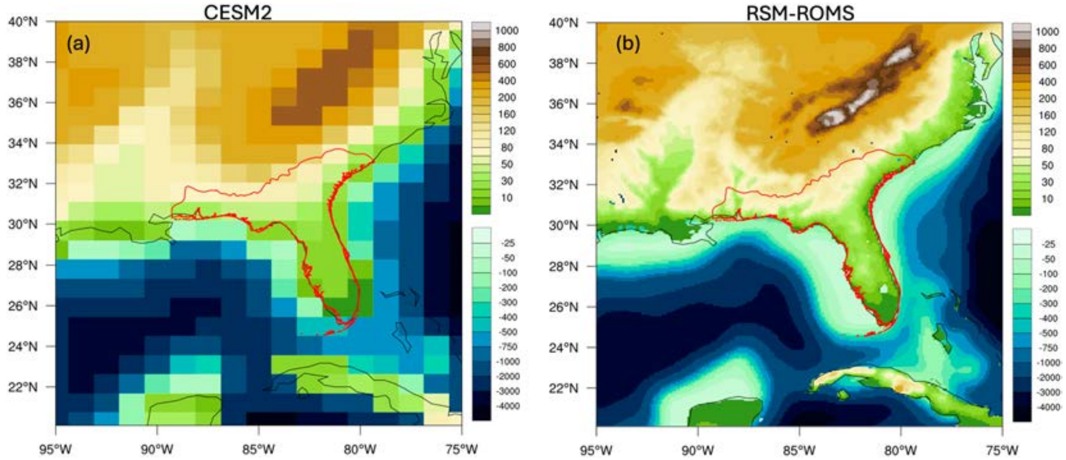

FIG. 1. The bathymetry (negative height) and topography (positive height in meters) from (a) CESM2 historical run and (b) RSM–ROMS at 10-km grid spacing with the outline of the FA overlaid in a red contour.

global climate models in the CMIP6 repository (e.g., Simpson et al. 2020; Meehl et al. 2020; Capotondi et al. 2020). For example, Simpson et al. (2020) indicate that large-scale atmospheric circulation in the Northern Hemisphere associated with jet streams, storm tracks, stationary waves, divergent circulation, and annular modes like the NAO has shown improvement in CESM2 compared to its previous generation and other CMIP6 models. Similarly, Capotondi et al. (2020) suggest that CESM2 displays ENSOs with realistic time scale, temporal evolution, and its teleconnections are also reasonably well represented including its pattern and seasonality.

The historical run (1850–2014) of CESM2 followed the protocols of CMIP6, as detailed in Eyring et al. (2016). The historical run of CESM2 with prescribed monthly evolving global concentrations of greenhouse gases, volcanic aerosols, and solar variability forcing (Simpson et al. 2023) is downscaled in this study. The RCM used in this study is the regional spectral model (RSM) coupled to the Regional Ocean Modeling System (ROMS; RSM–ROMS). This model has been widely adopted for conducting regional climate studies (e.g., Li et al. 2012, 2014; Ham et al. 2012; Misra et al. 2018; Jayasankar et al. 2023) and has been specifically adopted for regional climate studies of Florida (Misra and Mishra 2016; Misra et al. 2016, 2019).

In this study, we have centered the RSM–ROMS domain on the FA (Fig. 1b) with sufficient distance from the lateral boundaries in the zonal and meridional directions to avoid contamination from relaxation to the prescribed large-scale forcing at the lateral boundaries as is routinely done in RCMs (Davies 1976). For this study, RSM–ROMS is configured at 10-km grid spacing that is identical in its discretization in both RSM and ROMS. As a result, the fields are exchanged directly between these component models at intervals of 1 h (=coupling interval) without the use of any flux coupler. The size of the regional domain is 240 grid points in the zonal and 261 grid points in the meridional direction (Fig. 1b). The first evidence of the value of downscaling is apparent from Fig. 1, which shows a comparison of the bathymetry and topography between the global model (CESM2) and RSM–ROMS. The broad continental shelf along the Gulf Coast of United States is poorly resolved in CESM2. Furthermore, the coastlines are crude, and the topography of the Appalachians is shallow and broad in CESM2. RSM–ROMS at 10-km grid spacing significantly improves all these features, which will have an impact on its simulation as elaborated later in this study.

RSM, the atmospheric component model of the RCM, follows originally from Juang and Kanamitsu (1994). The RSM has a spectral core to solve the primitive equations that predicts the total field of winds, temperature, natural log of surface pressure, specific humidity, and cloud liquid water. The RSM separates each of its prognostic field as the linear sum of the time tendency of the base field representing the large-scale forcing and the time tendency of a perturbation field that is obtained as the difference between the RSM prediction and global model/reanalysis forcing. The RSM imposes a wall boundary condition or no slip condition to the perturbation tendency components of the wind field where the boundaries are treated as rigid walls following Tatsumi (1986). Additionally, RSM also uses a spectral damping scheme to ameliorate the systematic errors of RSM or its tendency to drift away from the large-scale forcing (Kanamaru and Kanamitsu 2007). This spectral damping scheme also allows for larger than commonly adopted nesting ratios. The RSM uses a semi-implicit time integration scheme, and for this study, we used a time step of 30 s. It has 28 terrain following sigma levels with the top of the atmosphere ~2 hPa. The atmospheric physics package used in RSM for this study is outlined in Table 1.

The datasets of soil type, vegetation type, and vegetation fraction are interpolated and made consistent with the land–ocean mask interpolated to the RSM grid from the Global 30 Arc-Second Elevation (Danielson and Gesch 2011).

ROMS, the oceanic component model of the RCM, is a free surface and terrain following the primitive equation model (Haidvogel et al. 2000; Shchepetkin and McWilliams 2005). This model incorporates 30 vertical stretched terrain levels, with a focus on enhancing resolution in the upper ~500 m of the ocean. The horizontal grid employed in the ROMS follows

TABLE 1. Outline of the atmospheric physics in RSM.

Physical parameterization	Reference
Land surface	Ek et al. (2003)
Boundary layer	Hong and Pan (1996)
Deep convection	Kain and Fritsch (1993) and Kain (2004)
Shallow convection	Tiedtke (1983)
Shortwave radiation	Chou and Lee (1996)
Longwave radiation	Chou and Suarez (1994)
Gravity wave drag	Alpert et al. (1988)
Clouds (explicit)	Zhao and Carr (1997)

the staggered Arakawa C grid configuration. Various parameterizations are integrated into the ROMS, which include local closure schemes based on the level 2.5 turbulent kinetic energy equations (Mellor and Yamada 1982), a boundary layer formulation rooted in the nonlocal closure scheme (Large et al. 1994), second-order biharmonic horizontal diffusion (Ezer et al. 2002), and a generic length scale parameterization (Umlauf and Burchard 2003). In this study, a time step of 300 s is utilized for the ROMS, ensuring precise and detailed simulations of oceanic processes. The ocean bathymetry used in the ROMS is from 2-min gridded global relief data from NOAA National Geophysical Data Center (2006). The orography over land and the bathymetry in the ocean for the RSM–ROMS domain and resolution used in the study with notable features labeled are shown in Fig. 1.

The initial and lateral boundary conditions of the atmosphere and the ocean are supplied to RSM–ROMS from the CESM2 historical run. The initial and boundary conditions are interpolated to the RSM–ROMS grid. The lateral boundary conditions of RSM are provided at intervals of 6 h from CAM6 of the CESM2 historical run. The ocean lateral boundary conditions are provided from POP2 to ROMS at monthly interval. The RSM–ROMS is integrated from 1 January 1985 through 31 December 2014.

3. Verification data

As stated earlier, the verification of the RSM–ROMS simulation of the current climate is one of the objectives of this study. Therefore, the verification data used in the study are outlined in Table 2.

It may be noted that in comparing the model simulation to the observations, we linearly interpolated the model simulations to the observed grid when computing the differences between them. Otherwise, the fields were plotted on their original grids. Furthermore, the analysis of the CESM2 historical run is for the overlapping period of 1985–2014 of the RSM–ROMS integration.

The satellite-based rainfall analysis used in this study is also used to validate the diurnal variations of precipitation from the model. This NASA IMERG product used in this study has been validated at the diurnal scales, which indicate that its fidelity is comparable to the available in situ observations in the southeastern United States (Tan et al. 2019). Furthermore, the CESM2 historical simulations of CMIP6 failed to provide their model output at subdaily intervals to evaluate its diurnal variations. In

TABLE 2. Verification datasets used in the study.

Variable	Source	Purpose	Temporal resolution	Spatial resolution	Period used in the study
SST	OISSTv2 (Reynolds et al. 2007)	Verification of seasonal mean SST and rainfall–SST relationship	Daily	0.25° × 0.25°	1985–2014
Depth of the 20°C isotherm in the ocean	SODA reanalysis (Carton and Giese 2008)	Verification of the depth of the seasonal mean 20°C	Monthly	0.5° × 0.5°	1985–2010
Surface ocean currents	HYCOM-GOFS3.1 reanalysis (HYCOM 2024)	Verification of surface currents and mixed layer depth	Monthly	1/12° with 0.08° × 0.08° between 40°S and 40°N	1994–2015
Sea surface height	AVISO (https://www.aviso.altimetry.fr/en/home.html)	Verification of GEKE	Monthly	1/8°	1993–2022
Upper-air variables	ERA5 (Hersbach et al. 2019)	Verification of seasonal mean 850-hPa winds, precipitable water	Monthly	0.25° × 0.25°	1985–2014
Rainfall	IMERG v7 (Huffman et al. 2023, 2024)	Verification of seasonal mean, interannual, daily, and diurnal variations in rainfall	Half hourly	0.1° × 0.1°	2001–23
Land surface temperature	CPC Global Unified Temperature (CPC 2024)	Verification of seasonal mean, interannual, and daily variations in surface temperature	Daily	0.25° × 0.25°	1985–2014
TC fixes	NHC "best track" hurricane database (HURDAT2; Landsea and Franklin 2013)	Verification of TC genesis and tracks	6 hourly		1985–2014

addition, the variables available at daily interval from the CESM2 integration are also limited. These limitations also highlight the benefit of dynamic downscaling since we can customize to provide higher temporal resolution data in the absence of such data from the driving global model in addition to the higher spatial resolution from the RCM.

4. Results

a. *Climatology*

PRECIPITATION AND SURFACE TEMPERATURE

The seasonal climatology of observed precipitation is shown in Figs. 2a–d, and the corresponding systematic errors from CESM2 are shown in Figs. 2e–h and from RSM–ROMS in Figs. 2i–l. The seasonal climatological precipitation from CESM2 and RSM–ROMS is shown in Fig. S1 in the online supplemental material. The seasonal variation in the precipitation over the FA is the most significant in the regional domain, with the annual minimum in the winter of DJF (Fig. 2a) and annual peak in the summer of JJA (Fig. 2c). This seasonal variation in precipitation is comparatively weak in CESM2 (Figs. S1a–d), while the observed seasonal precipitation seasonal cycle is mostly restored in RSM–ROMS (Figs. S1e–h). The dry bias over the FA in the summer in CESM2 (Fig. 2g) is significantly reduced in RSM–ROMS (Fig. 2k). In the other three seasons of the year, the wet bias over the FA is slightly more severe in RSM–ROMS compared to CESM2 (Fig. 2 and Fig. S1). The wet and dry bias in the surrounding oceans in DJF and JJA appears to be more severe in RSM–ROMS in Figs. 2i and 2k compared to CESM2 in Figs. 2e and 2g, respectively. It may be noted that the systematic errors of the seasonal precipitation in both CESM2 and RSM–ROMS in Fig. 2 and Figs. S1i–l are considerably reduced in comparison with Bhardwaj and Misra (2019; cf. Fig. 3; especially, the severe dry bias over peninsular Florida in the summer season). The comparison here is relevant because Bhardwaj and Misra (2019) downscaled CCSM4 (a previous generation of CESM2) with a slightly different version of RSM–ROMS (using a different cumulus parameterization scheme) run at 10-km grid spacing albeit, on a much smaller domain than the current study.

The seasonal cycle of the hydroclimate of Florida is closely tied to the seasonal cycle of the Loop Current and the evolution of the SST in the neighboring oceans (Misra and Mishra 2016; Misra et al. 2017b). In fact, it is shown that changes in the SST, especially over the west Florida shelf, have a significant impact on the hydroclimate of Florida (Misra and Bhardwaj 2021). The study indicates that the SSTs in the west Florida shelf affect the moisture flux convergence, which, in turn, impacts the precipitation over peninsular Florida in the JJA season.

It is interesting to note that both in the observations and in the RSM–ROMS simulation, the predominant north-to-south gradient of precipitation over the FA over most of the seasons is dominated by the east-to-west gradient between the coasts of peninsular Florida in the summer. This is typical of the summer season, where the southwesterly moisture flux of the Bermuda high dominates and feeds the persistent diurnal variability of sea-breeze thunderstorms in southwestern Florida (Bastola and Misra 2013; Misra and Bhardwaj 2022).

The seasonal cycle of the surface temperature over land (2-m air temperature) and the ocean (bulk SST) also shows a robust seasonal cycle with DJF being the coldest and JJA being the warmest (Figs. 3a–d). This is captured both in CESM2 (Figs. S2a–d) and in RSM–ROMS (Figs. S2e–h). Nonetheless, the CESM2 shows a warm bias over both land and the oceans, especially the coastal oceans of CESM2 around the FA (Figs. 3e–h). This bias is significantly ameliorated in RSM–ROMS (Figs. 3i–l). However, the cold bias along the coastal oceans in RSM–ROMS is more severe than in the rest of the domain (Figs. S2i–l). In the case of CESM2, the coastal bathymetry is poorly resolved, especially of the west Florida shelf compared to RSM–ROMS, which leads to significant issues in resolving or permitting the Loop Current and their eddies in the historical run of CESM2 (Misra et al. 2019). Furthermore, the SST in the coastal oceans of CESM2 is not well defined and, as a result, depicted by "white spaces" in the differences with the observed SST in Figs. 3e–h. It may be noted that the verification data for SST are at 0.25° grid resolution, which is ~2.5 times coarser in resolution than RSM–ROMS. Additionally, the Gulf of Mexico region, especially the west Florida shelf region, is not a well-observed region of the global oceans (Muller-Karger et al. 2015; Weisberg et al. 2016). As a result, the SST analysis is dependent on satellite estimates over the region, which is often covered by low-level clouds (Wang and Enfield 2001; Misra and DiNapoli 2013; Misra and Bhardwaj 2022), which raises the uncertainty of their retrievals. In comparison with Bhardwaj and Misra (2019), the SST simulations of the current study over the west Florida shelf and along the Atlantic coast of Florida show considerable improvement in both CESM2 and RSM–ROMS. For instance, the cold bias along the Atlantic coast and the western edge of the west Florida shelf and the warm bias over the west Florida shelf in RSM–ROMS in Bhardwaj and Misra (2019; cf. Fig. 2) are reduced, especially in the fall and winter seasons. Likewise, CESM2 also shows similar improvements over CCSM4.

The seasonal climatology of SST and surface air temperature reveals several mesoscale features in RSM–ROMS (Fig. 3 and Fig. S2), which verifies with the corresponding observations. For instance, the relatively cooler temperatures over the Appalachian Mountains across all seasons align more naturally along the orography in RSM–ROMS like the observations. Similarly, the SST gradients in the Gulf of Mexico aligned with the Loop Current circulation in the observations (Figs. 3a–d) are also evident in the RSM–ROMS simulation (Figs. S2e–h).

Similarly, the seasonal cycle of the precipitable water follows a similar cycle as precipitation with the moisture content in the atmospheric column over the FA being the lowest in DJF and highest in JJA (Figs. S3a–d). Furthermore, the north-to-south gradient of the precipitable water over the FA is like the precipitation and surface temperature gradients with it being weakest during the summer. In addition, the gradients of precipitable water surrounding the Appalachian Mountains across all the seasons are nicely captured in the RSM–ROMS

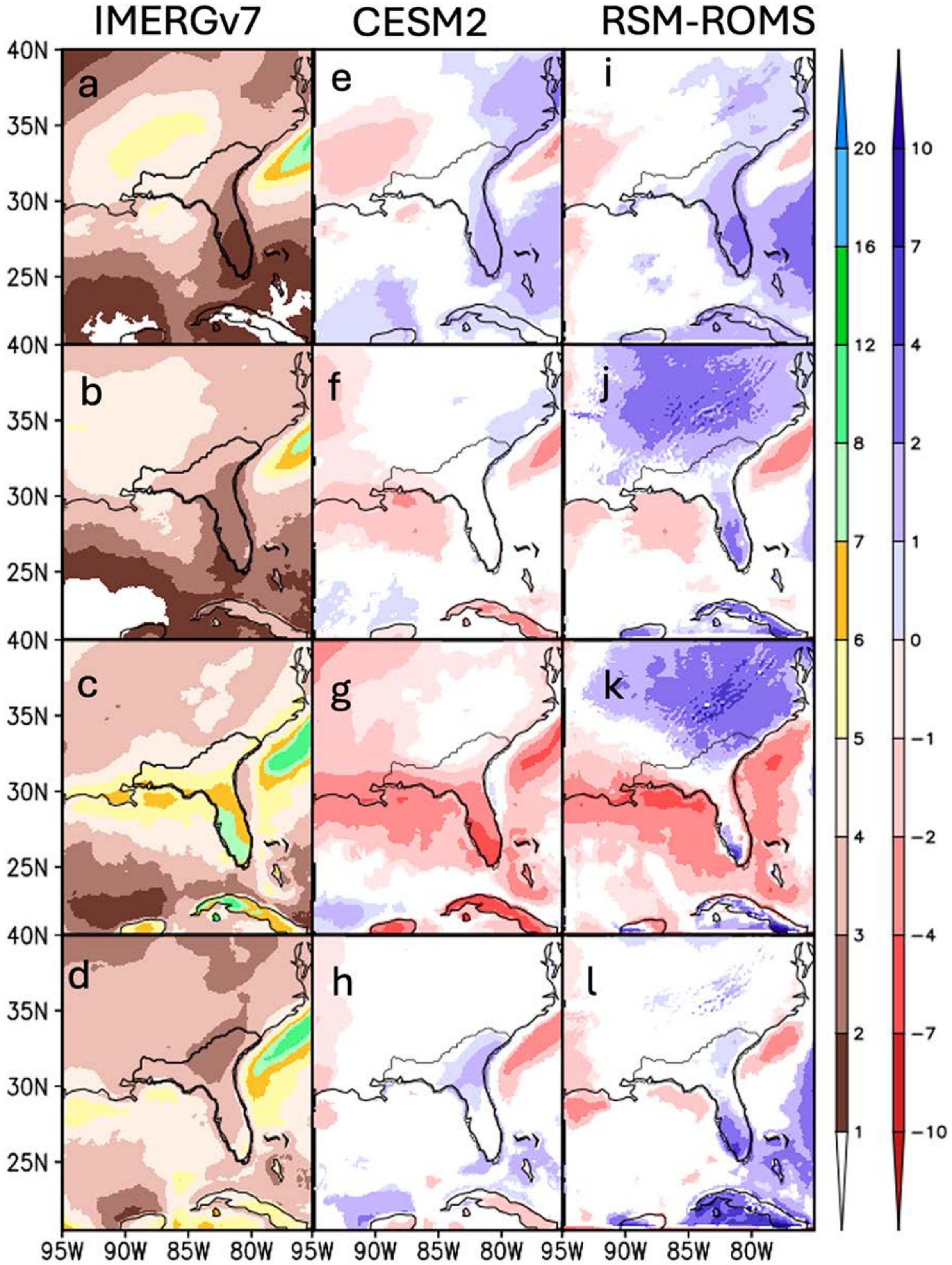

FIG. 2. The seasonal climatology of rainfall (mm day^{-1}) from (a)–(d) observations (IMERGv7) and the corresponding systematic errors (mm day^{-1}) from (e)–(h) CESM2 and (i)–(l) RSM–ROMS for (a),(e),(i) DJF, (b),(f),(j) MAM, (c),(g),(k) JJA, and (d),(h),(l) SON seasons. Only significant values at 5% significance level according to the *t* test are shaded for the differences. The outline of the FA is overlaid in a thick black contour.

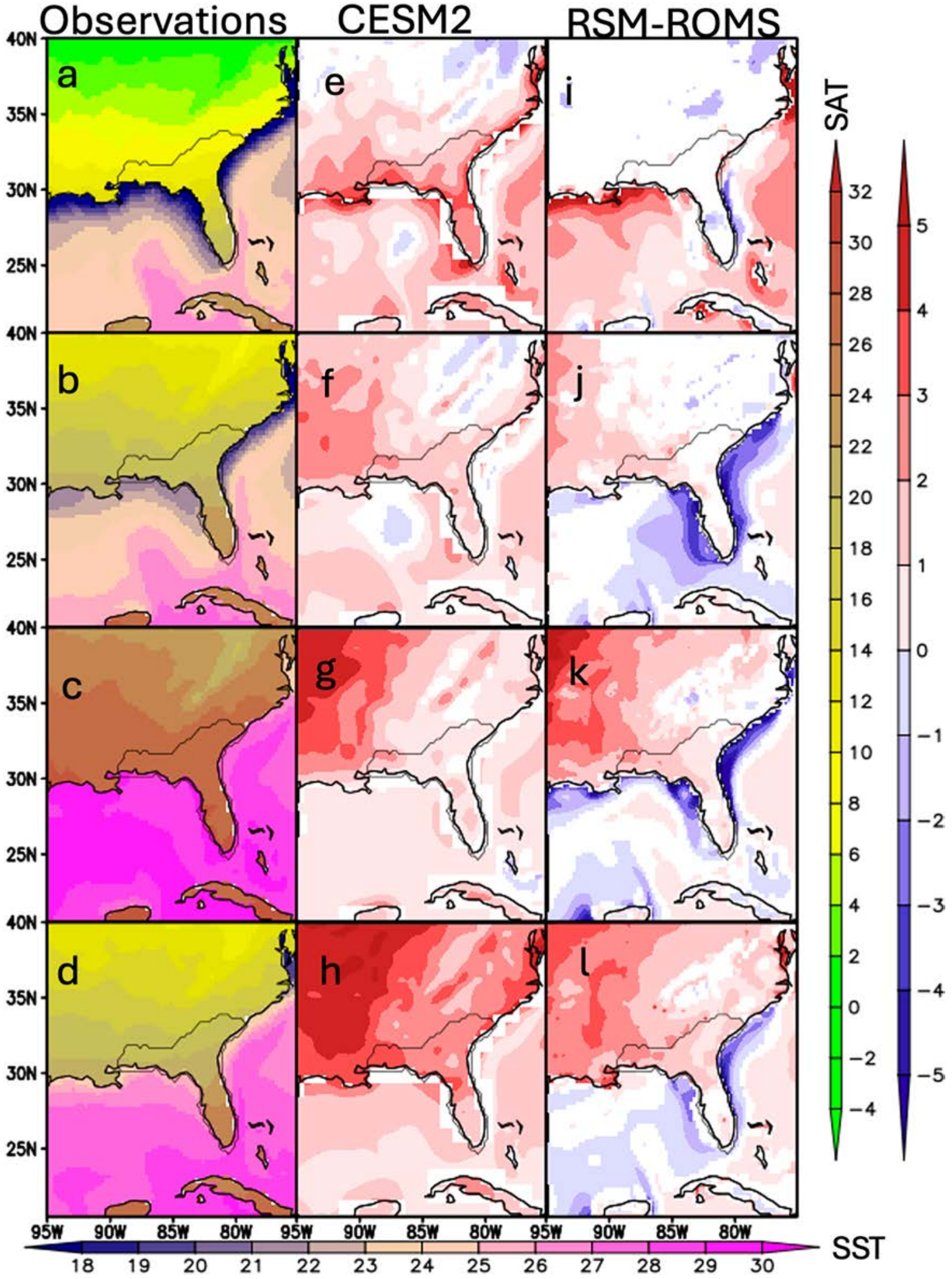

FIG. 3. The seasonal climatology of surface temperature (°C) from (a)–(d) observations [OISSTv2 bulk SST and CPC SAT over land], and corresponding systematic errors from (e)–(h) CESM2, and (i)–(l) RSM–ROMS for (a),(e),(i) DJF, (b),(f),(j) MAM, (c),(g),(k) JJA, and (d),(h),(l) SON seasons. Only significant values at 5% significance level according to the *t* test are shaded for the differences. The outline of the FA is overlaid in a thick black contour.

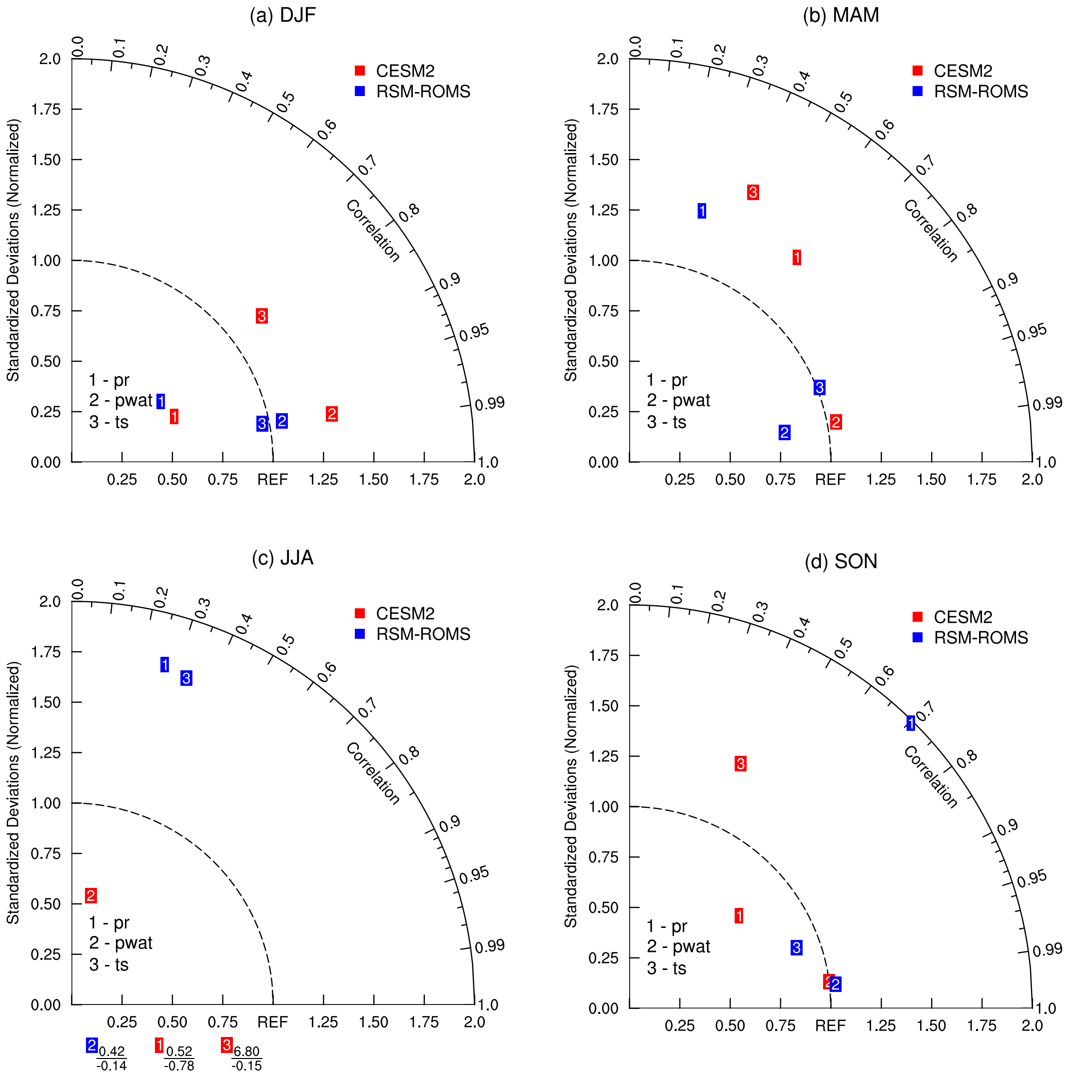

FIG. 4. Standardized Taylor diagram for (a) DJF, (b) MAM, (c) JJA, and (d) SON seasonal mean from RSM–ROMS and CESM2 simulations for precipitation (pr), precipitable water (pwat), and surface temperature (ts) over the FA. The blue and red squares represent RSM–ROMS and CESM2, respectively. The ratios indicated in (c) are out of range on display and show the ratio of the standard variances to correlation coefficients.

simulation, especially during the spring and fall seasons of MAM and SON, respectively. Once again, we note that the seasonal bias of precipitable water over the FA is reduced in RSM–ROMS compared to CESM2 except in the summer when the former exhibits a severe dry bias (Fig. S4).

An objective comparison of these variables using the Taylor diagram (Fig. 4) indicates that RSM–ROMS is superior to CESM2 as an aggregate over the FA in terms of the seasonal climate of precipitation, surface temperature, and precipitable water across most seasons. For example, the pattern correlations of precipitation and surface temperature are higher in RSM–ROMS than CESM2 in all seasons except in the spring season. Similarly, the standardized variance is closer to the unit circle in the case of RSM–ROMS for all three variables with exceptions of precipitation in the fall and precipitable water in the summer when CESM2 is closer to the unit circle. It is important to note here that in the overall evaluation of an RCM, even a comparable skill of the large scale as the driving global model is considered a benefit if the permitted or resolved (mesoscale) details are exhibited with better skill (Staniforth 1997; Laprise et al. 2008; Davies 2014). In this case, RSM–ROMS shows some significant reduction in the seasonal bias of these variables over the FA while developing mesoscale gradients that verify with observations (Figs. S1, S2, and S4).

The seasonal climatology of the mixed layer depth overlaid with corresponding surface ocean currents is shown in Fig. 5. The surface ocean Loop Current is apparent from the ocean reanalysis in Figs. 5a–d, which also constitutes the upper branch of the Atlantic meridional overturning circulation (AMOC) transporting warm water from the Caribbean Sea into the Gulf of Mexico through the Yucatan Channel. This is simulated in both the model simulations (Figs. 3e–l). However,

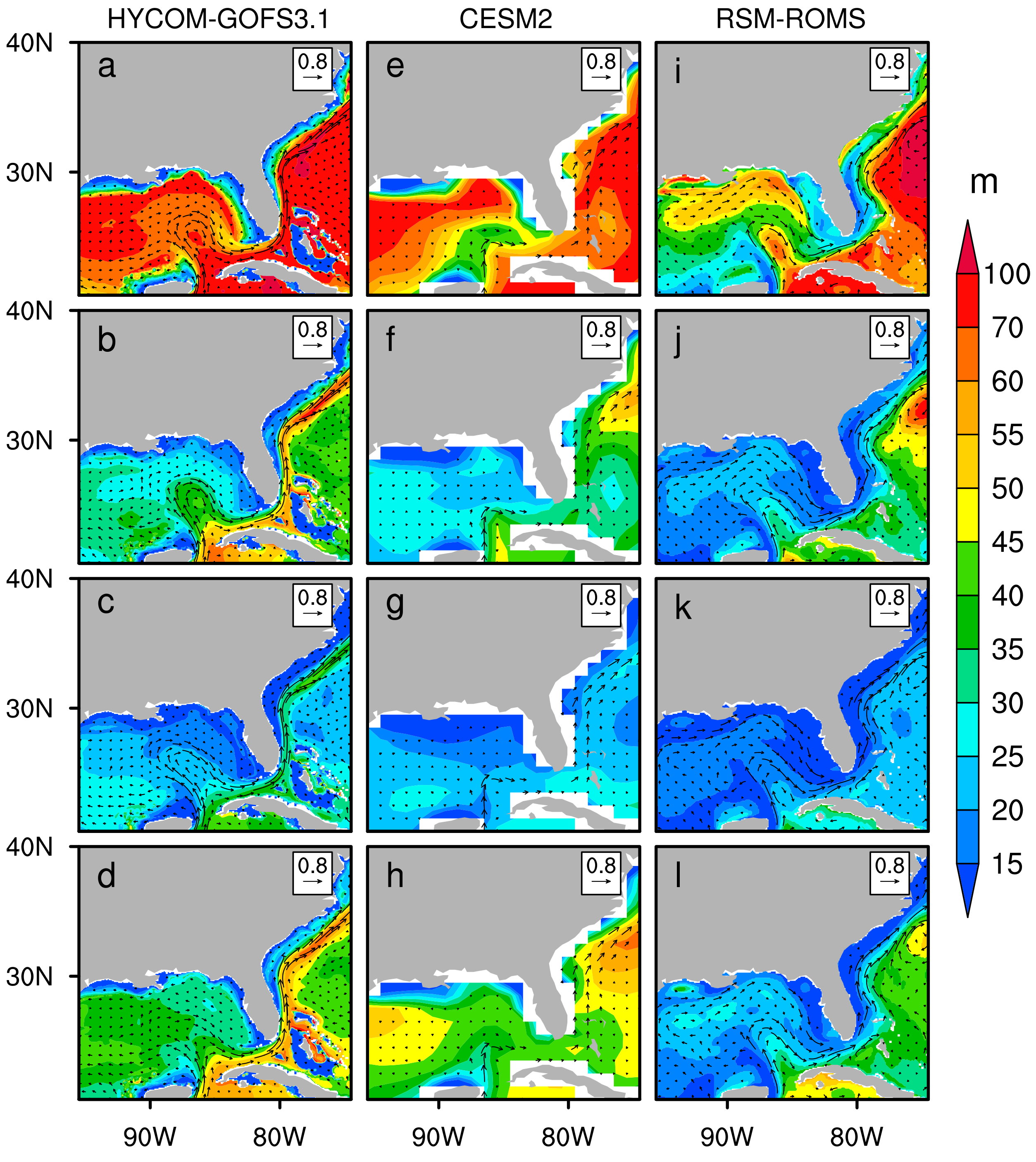

FIG. 5. The seasonal climatology of surface ocean currents (m s^{-1}) and mixed layer depth (m; shaded) from (a)–(d) observations (HYCOM-GOFS3.1 reanalysis), (e)–(h) CESM2, and (i)–(l) RSM–ROMS for (a),(e),(i) DJF, (b),(f),(j) MAM, (c),(g),(k) JJA, and (d),(h),(l) SON seasons.

the tilt and the northward intrusion of the Loop Current into the Gulf of Mexico is more prominent in the RSM–ROMS simulation, while these features are largely absent in the CESM2 simulation. Some studies point out that the seasonality of the Loop Current is poorly simulated in the global models because of the inadequate resolution (Liu et al. 2015; Misra et al. 2016). In fact, it is suggested that a grid resolution of 20 km or less is required for permitting Loop Current and their eddies in the model simulations (Hurlburt and Thompson 1980; Chérubin et al. 2005). The seasonality of the mixed layer is prominent with it being deepest in the winter and shallowest in the summer (Figs. 5a–d). This is largely simulated in both models,

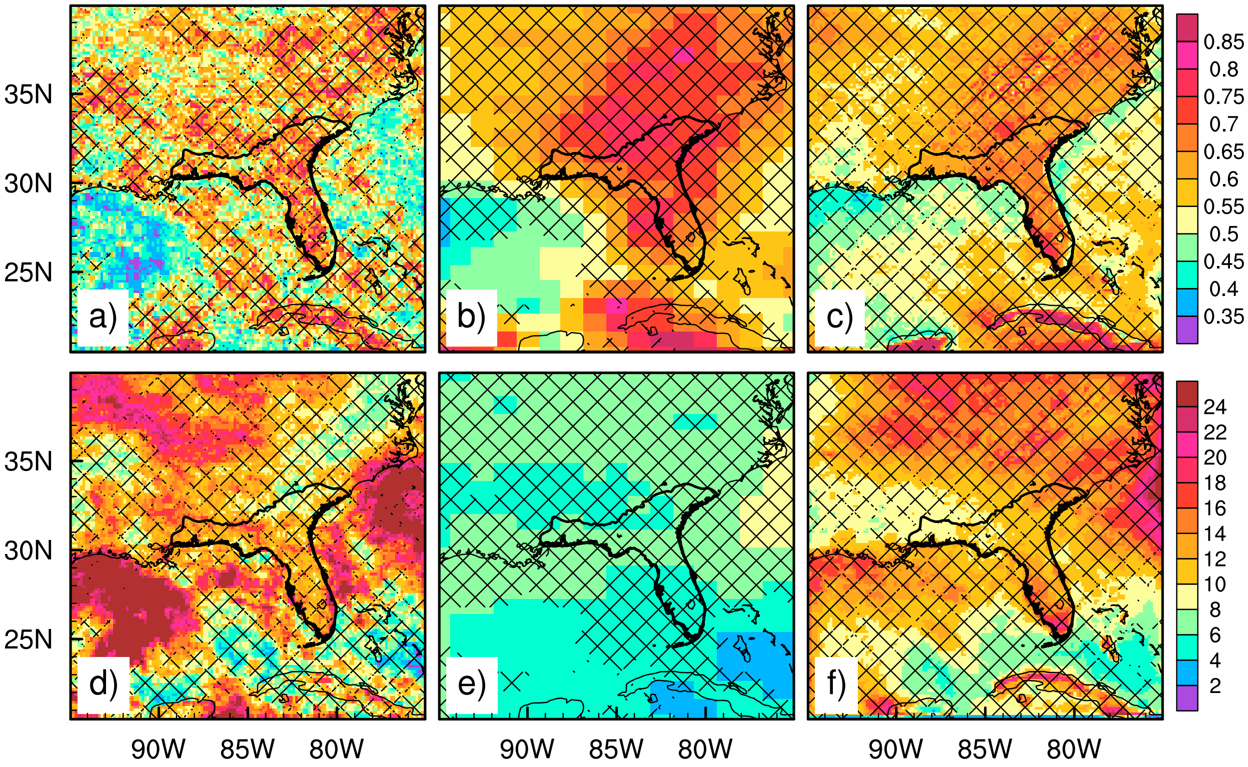

FIG. 6. The (a)–(c) shape and (d)–(f) scale (mm day^{-1}) parameters of the fitted gamma distribution of daily rainfall in JJA from (a),(d) IMERG, (b),(e) CESM2, and (c),(f) RSM–ROMS. The hatched regions indicate that the gamma distribution passes the goodness of fit according to the chi-squared test at 95% significance level. The outline of the FA is overlaid in a thick black contour.

although there are important subtle differences from observations as well as between the models. For instance, the mixed layer depth around the Loop Current in CESM2 exhibits a shallow bias that is ameliorated in RSM–ROMS. On the other hand, RSM–ROMS exacerbates the shallow bias of the mixed layer depth compared to CESM2 in the fall season from a slower seasonal recovery from the preceding summer compared to reanalysis or CESM2.

b. *High-frequency variability*

We examined the distribution of daily rainfall by fitting a gamma distribution to the rainy days in JJA (see ST1 in the supplemental section for the description of the methodology). Gamma distribution is widely used to fit the distribution of the daily rainfall given its versatility in accommodating a variety of shapes (Wilks 2006; Becker et al. 2009; Shi and Misra 2020). The two critical parameters of the gamma distribution are the shape and scale parameters, the product of which produces the mean daily rainfall. The shape parameter determines the skewness of the distribution. However, with the shape parameter being <1 in Figs. 6a–c, it suggests a highly skewed distribution in observations and the model simulations, which implies many low rainfall days interspersed with moderate to heavy rain events characterizes the summer season over the domain. In fact, the shape parameter being <1 even suggests that the distribution is exponential. The observations in Fig. 6a show a shape parameter that is more uniform across the FA and outside of FA, over a large terrestrial part of the domain. CESM2 in Fig. 6b shows a comparable distribution of the shape parameter although it overestimates it across the FA and most of the other terrestrial regions of the domain, which suggests that its daily distribution of rainfall is less exponential than observations. In other words, the CESM2 shape parameter of daily rainfall in Fig. 6b is already suggesting a lesser frequency of moderate to heavy rainfall events. On the other hand, RSM–ROMS shows a much-improved shape parameter in Fig. 6c compared to CESM2 in Fig. 6b. However, the shape parameter is slightly overestimated over the western Atlantic Ocean in RSM–ROMS but is yet an improvement over CESM2. Impressively, the RSM–ROMS simulation has a comparable JJA daily rainfall distribution along the coastal oceans of the FA as observations.

The scale parameter, which determines the typical rainfall amount per rain event, shows that the FA and the surrounding oceans in JJA exhibit large values in the observations (Fig. 6d). In contrast, CESM2 grossly underestimates the scale parameter across the domain (Fig. 6e). In comparison, RSM–ROMS shows comparable values of the scale parameter over the FA and the surrounding oceans compared to the observations (Fig. 6f). However, RSM–ROMS overestimates the scale parameter over the Appalachians and east of it while severely underestimating over the Gulf of Mexico, south of Louisiana. It may be noted that Berner et al. (2012) indicate that increasing model resolutions alone may not be necessarily beneficial in improving

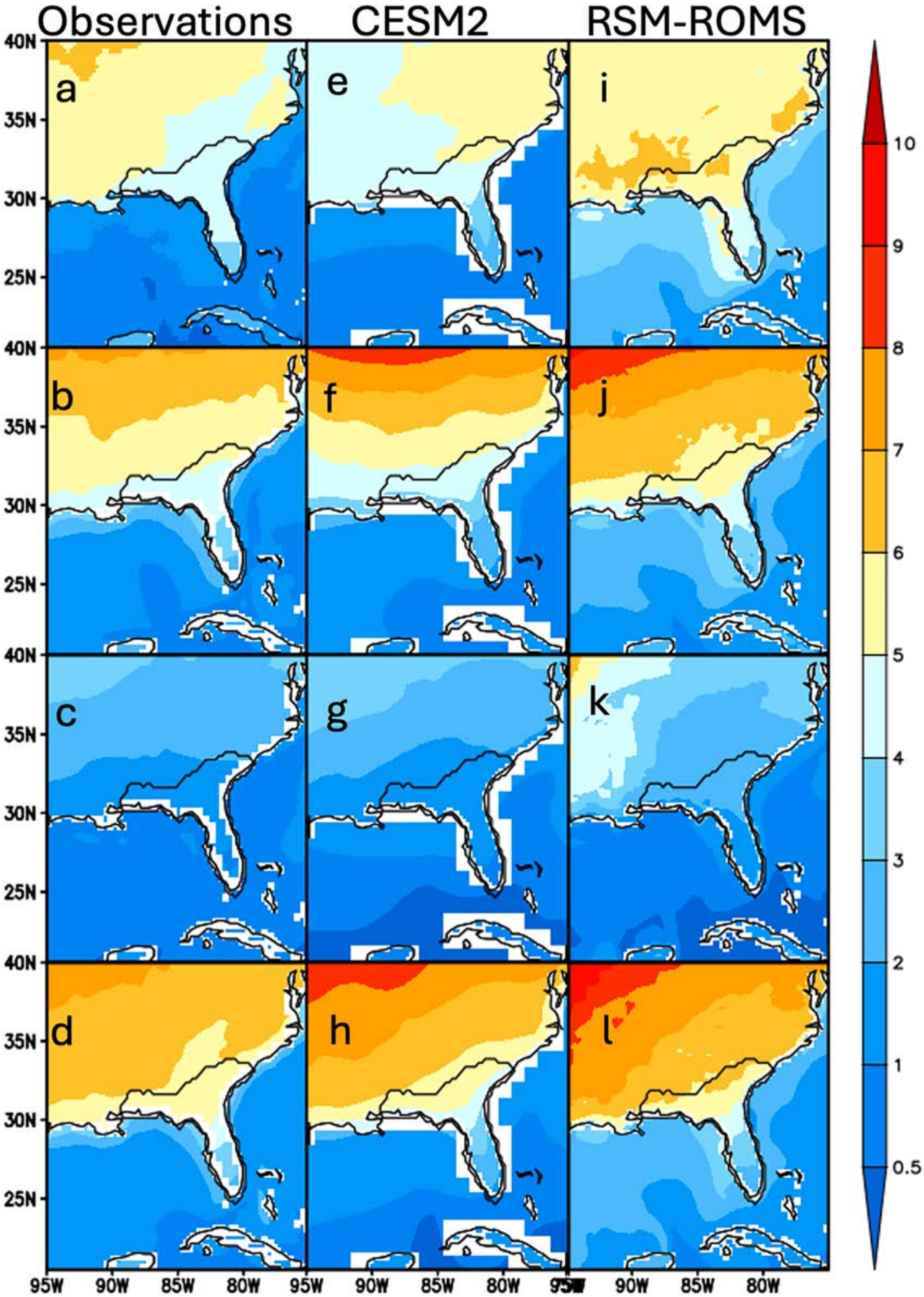

FIG. 7. The standard deviation of daily surface air temperature (°C) and SST (°C) seasonally averaged from (a)–(d) observations and (e)–(h) CESM2 and (i)–(l) RSM–ROMS for (a),(e),(i) DJF, (b),(f),(j) MAM, (c),(g),(k) JJA, and (d),(h),(l) SON.

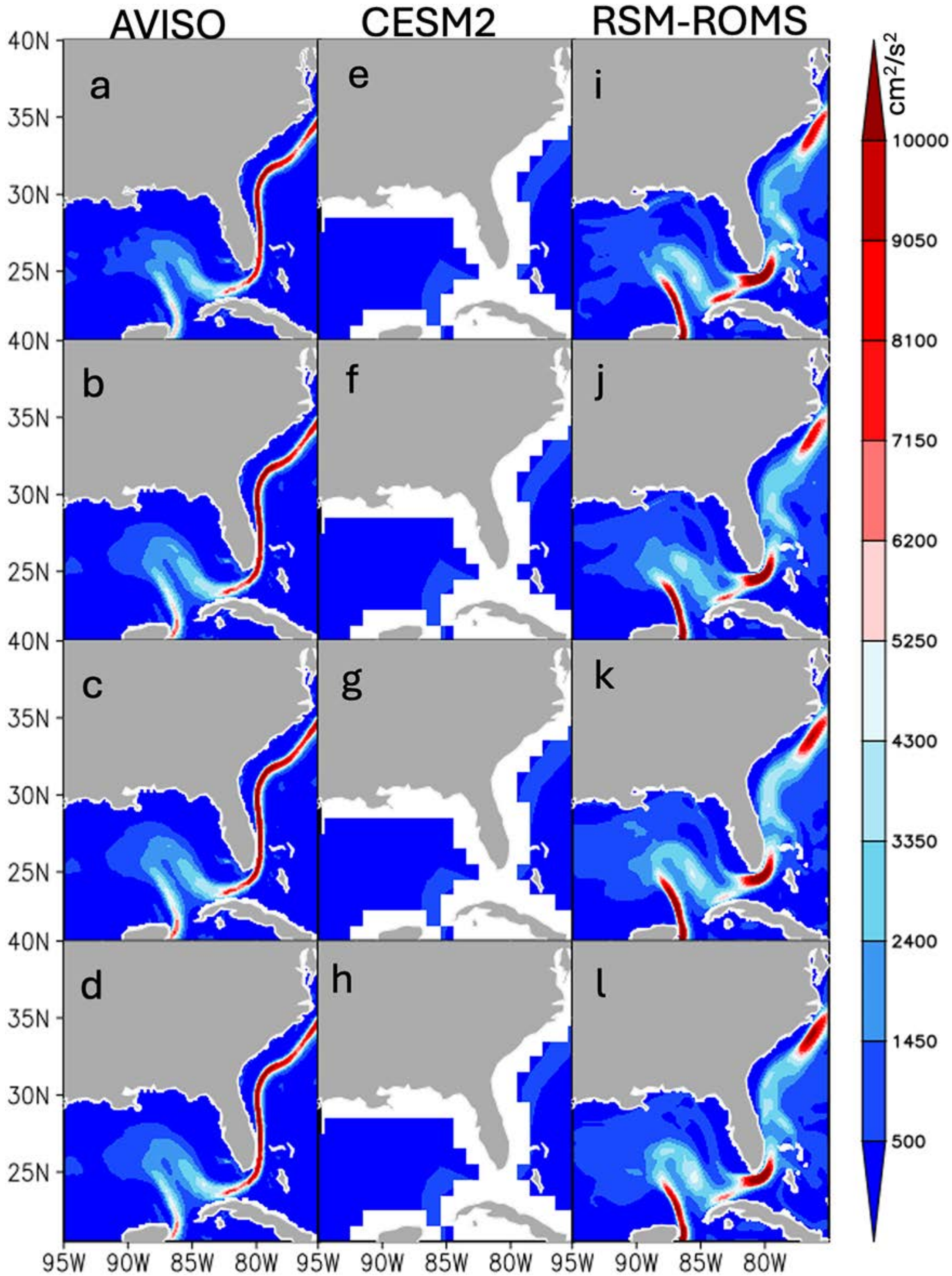

FIG. 8. The GEKE (cm^2 s^{-2}) from (a)–(d) observations (AVISO), (e)–(h) CESM2, and (i)–(l) RSM–ROMS for (a),(e),(i) DJF, (b),(f),(j) MAM, (c),(g),(k) JJA, and (d),(h),(l) SON.

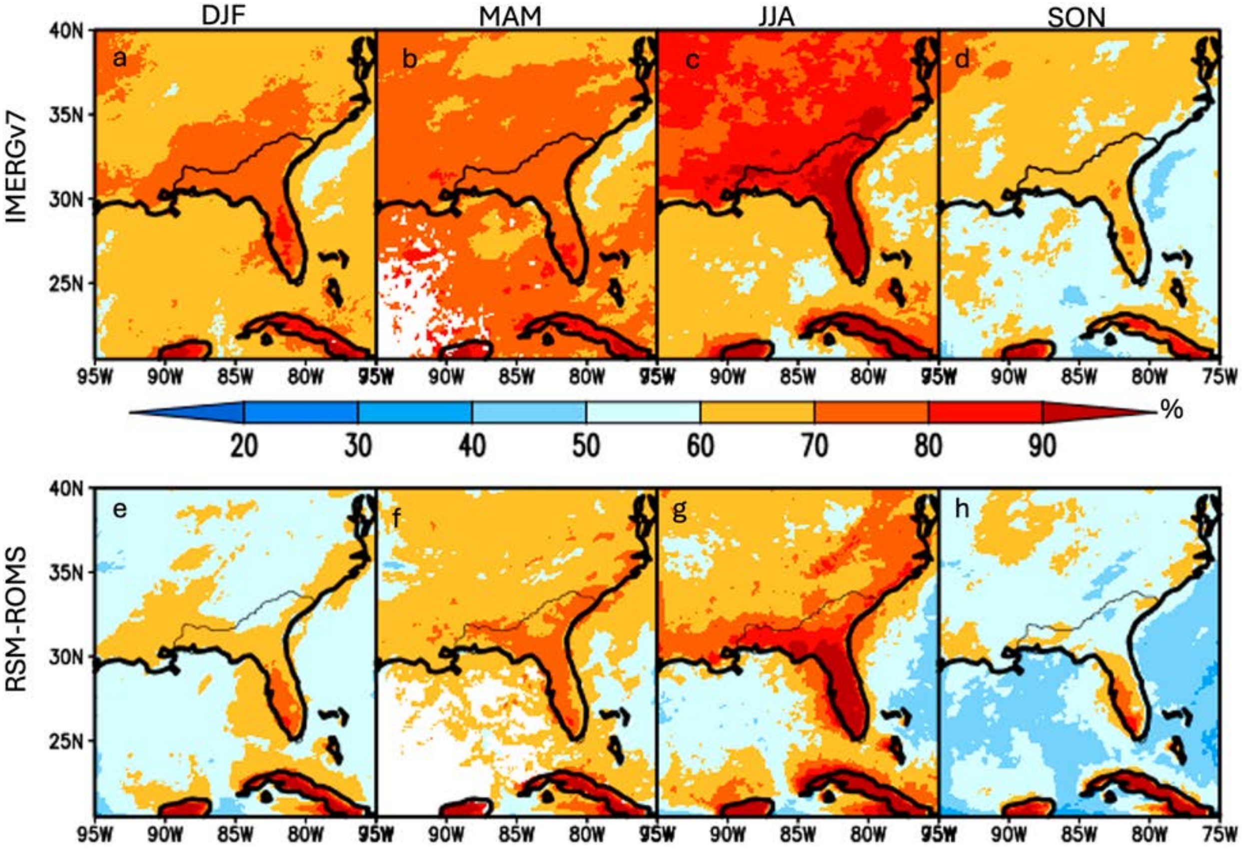

FIG. 9. The percentage of daily variance explained by the diurnal variation in precipitation for (a),(e) DJF, (b),(f) MAM, (c),(g) JJA, and (d),(h) SON seasons from (a)–(d) IMERG and (e)–(h) RSM–ROMS. The outline of the FA is overlaid in a thick black contour. The white space indicates that the diurnal variability of precipitation is undefined.

atmospheric convection features and they argue for, additionally, improvement in the physical parameterizations schemes that represent the subgrid-scale variations better. Similarly, in a multimodel study of diurnal variations in precipitation, Dirmeyer et al. (2012) find that more than the changes in the horizontal resolution, the distinctive treatments of physics in the models can account for the differences in representing the diurnal cycle of precipitation across models. Therefore, we contend that the improved verification of RSM–ROMS in Fig. 6 may be a result of the model physics, performing better at this grid resolution of 10 km. However, it may be noted that the shape and scale parameters in IMERG are far more inhomogeneous than either of the two model simulations. This could suggest that daily rain in IMERG is likely from smaller spatial-scale weather systems in the summer than what either of the models produce in their simulations.

We also examined the distribution of the extreme rainfall expressed as the percentage of the number of wet days in JJA that exceeded the 90th (R90p) and 95th (R95p) percentile thresholds from IMERG, CESM2, and RSM–ROMS in Fig. S5. Most of the regional domain shows over 8% and over 3% for R90p and R95p in IMERG in Figs. S5a and S5d, respectively. This is slightly overestimated in CESM2 and RSM–ROMS. However, owing to the higher resolution of RSM–ROMS, the spatial gradients of this metric are more strongly apparent and are consistent with IMERG. Nonetheless, the biases in the two model simulations (CESM2 and RSM–ROMS) are similar (Fig. S5).

We examine the daily variance of the surface temperature both over land surface and ocean by each season in Fig. 7. The daily land surface temperature variations show the least variance in the over the FA compared to the rest of the terrestrial region in the domain (Figs. 7a–d). Furthermore, the standard deviation of the observed land surface temperature is least in the summer compared to the rest of the year. This is also observed in the model simulations (Figs. 7e–l). In Figs. 7i–l, however, RSM–ROMS shows a larger variance of surface temperature over land including that over the FA than observations or CESM2. But the spatial pattern of the variance of land surface temperature is comparable in both model simulations and observations. The daily variance of SST also appears comparable in both model simulations and observations. The variability of the SST around the Loop Current is underestimated in CESM2, which is improved upon in RSM–ROMS. The variance of the SST in the coastal oceans, especially along the west Florida shelf in RSM–ROMS is comparable with observations. But on account of the coarse spatial resolution of CESM2, the west Florida shelf is largely unresolved.

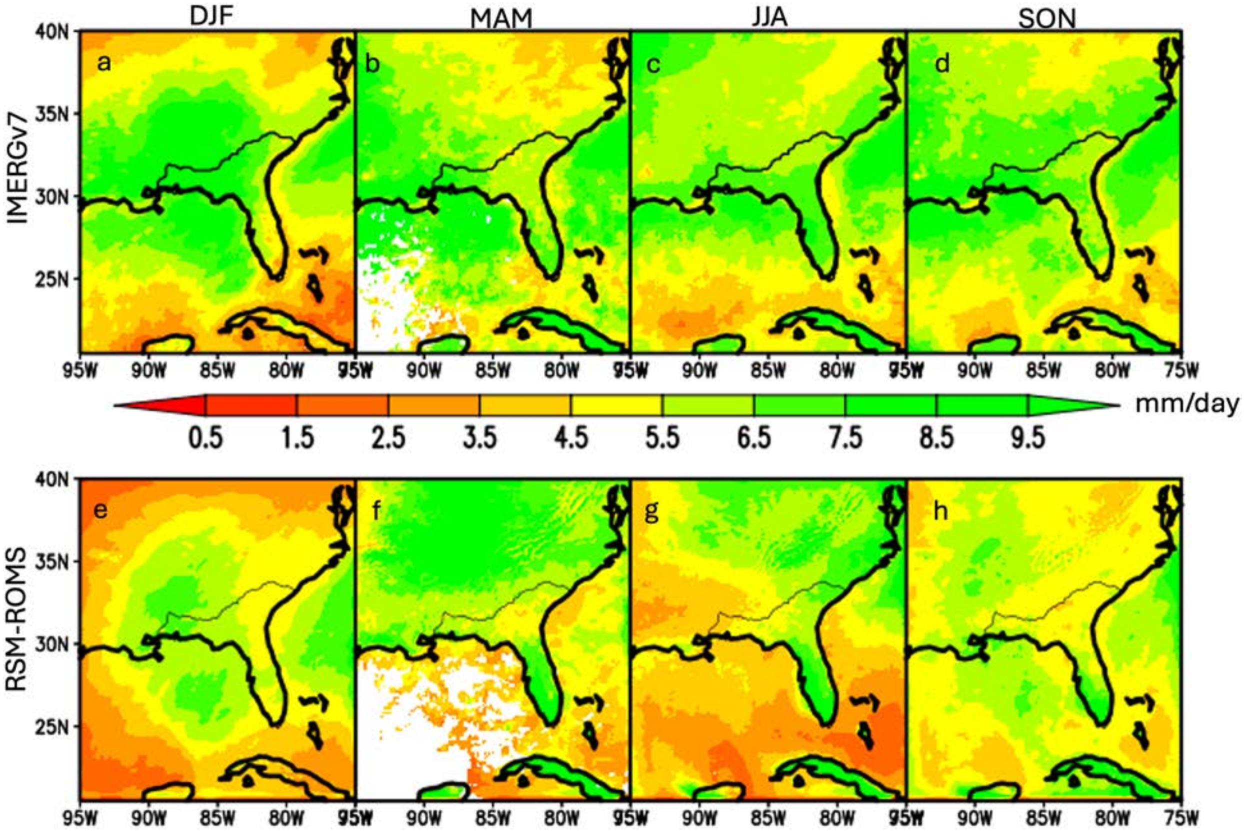

FIG. 10. The amplitude of the diurnal variation in precipitation (mm day^{-1}) for (a),(e) DJF, (b),(f) MAM, (c),(g) JJA, and (d),(h) SON seasons from (a)–(d) IMERG (black) and (e)–(h) RSM–ROMS. The outline of the FA is overlaid in a thick black contour. The white space indicates that the diurnal variability of precipitation is undefined.

In Fig. 8, we show the seasonal mean geostrophic surface eddy kinetic energy (GEKE) derived from the monthly mean sea surface height anomalies from observations, CESM2, and RSM–ROMS simulations. We did not have access to daily surface ocean currents from CESM2 historical simulation but had access to their daily sea surface height anomalies from which we could compute the GEKE (described in section ST2 of the supplemental section). It may be noted that GEKE is often used to study the variability of the oceans (e.g., Scharffenberg and Stammer 2010, Jouanno et al. 2012). Furthermore, we can compute the GEKE from satellite-derived sea surface height anomalies, an independent source of observations. The GEKE of the Loop Current system quantifies the turbulent energy associated with mesoscale eddies using geostrophic velocity anomalies. The Loop Current and its extension into the Gulf Stream is clearly visible by its large values and fine-scale structure of the GEKE in the observations that explains the mesoscale meanders about the mean flow (Figs. 8a–d). The GEKE is highest along the northern boundary of the Loop Current where meanders and eddy detachment often occur (Figs. 8a–d). There is also moderately elevated GEKE westward, from the northward edge of the Loop Current, where eddies from the Loop Current begin to drift slowly westward. However, the corresponding GEKE in CESM2 in Figs. 8e–h is weaker than the AVISO GEKE by an order of magnitude. This is not surprising given the coarse resolution of CESM2 and its bathymetry. This could be a grave error considering that the Loop Current and its eddies are an important component of the regional climate of this region (Misra et al. 2016). For instance, the warm core eddies of the Loop Current can sometimes become a critical influencing factor in the life cycle of some of the TCs (Shay et al. 2000). The RSM–ROMS simulation (Figs. 8i–l) nearly restores this surface eddy kinetic energy of this coastal current system from CESM2 and is comparable to the observations, although the underestimation of this variability along the western Atlantic coast is apparent.

c. *Diurnal variations in precipitation*

The diurnal variability of climate is one of the fundamental and the fastest modes of climate variations, especially of the terrestrial climate (Yang and Slingo 2001; Christopoulos and Schneider 2021). Furthermore, diurnal variability of precipitation is often used as a common benchmark for evaluating the performance of weather and climate models (Dai and Trenberth 2004; Dirmeyer et al. 2012; Christopoulos and Schneider 2021). These studies indicate that the diurnal variations in precipitation have been a constant challenge across generations of model development. The common bias across models has been that the mean diurnal precipitation is too early over land and the amplitude is weak over

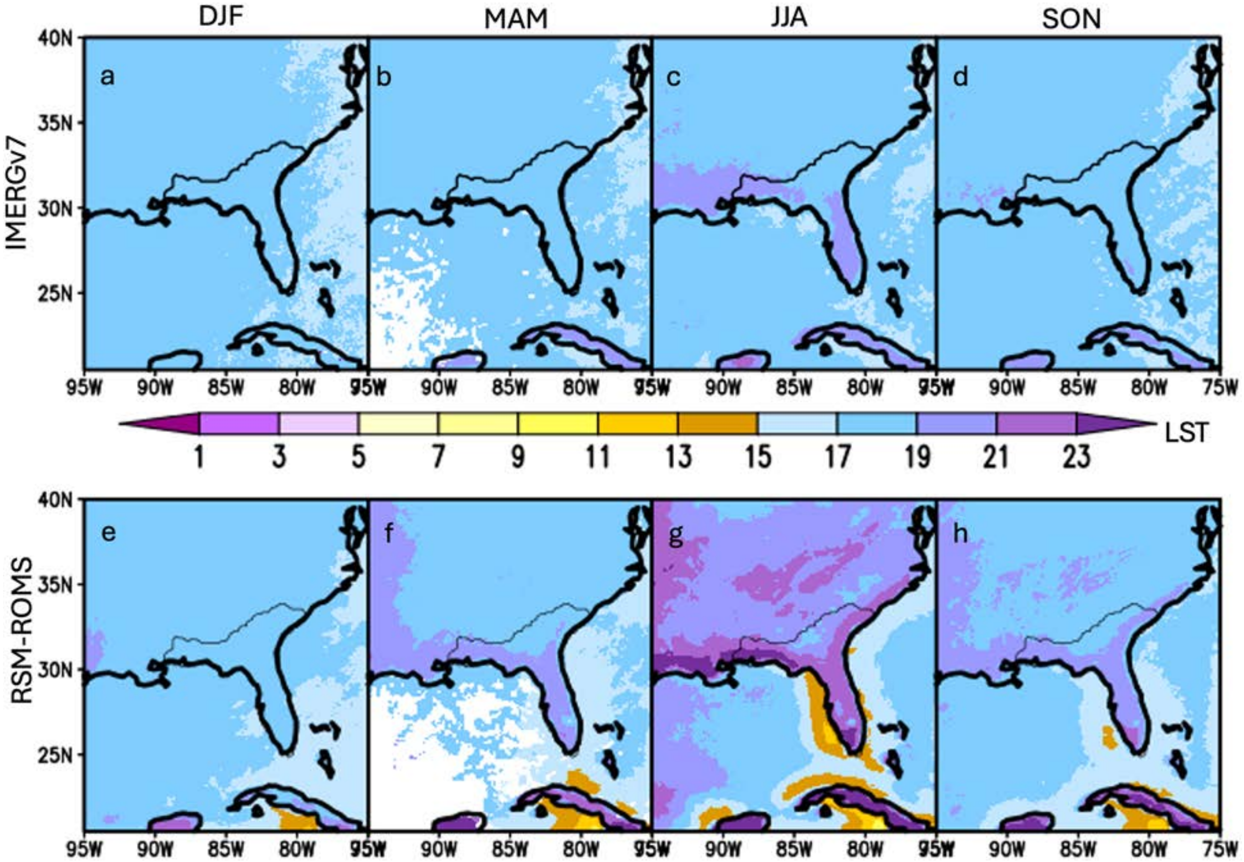

FIG. 11. The phase of the diurnal variation in precipitation [local standard time (LST)] for (a),(e) DJF, (b),(f) MAM, (c),(g) JJA, and (d),(h) SON seasons from (a)–(d) IMERG and (e)–(h) RSM–ROMS. The outline of the FA is overlaid in a thick black contour. The white space indicates that the diurnal variability of precipitation is undefined.

the oceans (Randall et al. 1991; Collier and Bowman 2004; Christopoulos and Schneider 2021).

Bastola and Misra (2013) indicated the importance of diurnal variation in precipitation on the seasonal mean precipitation across southeastern United States from observations. They showed that the volume error from calibrated hydrological models in some of the watersheds in the southeastern United States could be over 70% when subdaily rainfall is aggregated to daily rainfall on account of diminishing the influence of the diurnal variations in rainfall. In Fig. 9, we show the fraction of daily variance explained by the diurnal variability of precipitation for each of the four seasons from observations and RSM–ROMS. The observations show that diurnal variations explain over 60% of the daily variance across all four seasons (Figs. 9a–d). In fact, the summer season shows that the diurnal variations explain over 90% of the daily variance in Florida Peninsula and over 70% of the daily variance in other terrestrial parts of the domain (Fig. 9d). This is reasonably well simulated by RSM–ROMS, especially over the FA (Figs. 9e–h). It should be mentioned that the IMERG rainfall product used here for validation shows reasonable fidelity with multiradar multisensor rainfall analysis in the southeastern United States and in the coastal oceans (Tan et al. 2019). It is noteworthy that both the observations and RSM–ROMS show a relatively weaker fractional variance explained by diurnal variations over the oceans compared to the terrestrial regions of the domain. However, this contrast is stronger in the RSM–ROMS simulation. The unavailability of the historical CESM2 integration at subdaily intervals to diagnose the diurnal variability of precipitation has hampered us to compare its diurnal variability.

Similarly, we compare the diurnal amplitude of precipitation between the observations (Figs. 10a–d) and RSM–ROMS (Figs. 10e–h). The observations in Figs. 10a–d indicate that the seasonal diurnal amplitude of precipitation is pronounced over Peninsular Florida, along the Gulf and the Atlantic coasts. Furthermore, there is a distinct seasonality to the amplitude of the diurnal variations. For example, large parts of southeastern United States outside of the FA has the largest amplitude in the winter coinciding with its wet season (Figs. 10a,b). In comparison, Florida Peninsula shows its highest diurnal amplitude of rainfall in the summer (Fig. 10c). The RSM–ROMS simulation also displays a robust seasonal variability of the diurnal amplitude across the domain (Figs. 10e–h). It captures the annual peak of the diurnal amplitude of rainfall over Florida Peninsula in the summer. The RSM–ROMS,

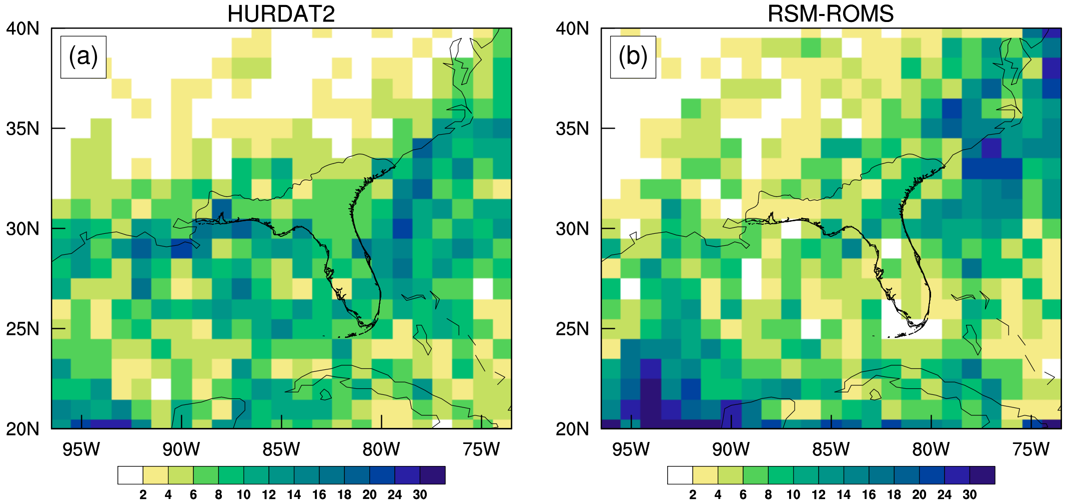

FIG. 12. The track density of named TCs (maximum sustained wind speeds ≥ 17 m s^{-1}) over a 30-yr period from (a) HURDAT2 and (b) RSM–ROMS simulation. The track density refers to TCs per 1° × 1° grid box per 6-h interval.

however, underestimates the diurnal amplitude in the southeastern United States outside of the FA in the winter (Fig. 10e), overestimates over the Appalachians in the spring (Fig. 10f), and underestimates over the Appalachians in the fall (Fig. 10h). Furthermore, RSM–ROMS tends to underestimate the diurnal amplitude of precipitation over the oceanic regions of the domain throughout the year. The observations show a gradient of diurnal amplitude of precipitation between the open ocean and the coastal oceans in the domain across all seasons. This is also seen in the RSM–ROMS simulation, albeit much weaker, with the amplitude along the coastal oceans being weaker than observations.

The phase of diurnal precipitation as ascertained by the time of the peak of diurnal precipitation from observations and RSM–ROMS is shown in Fig. 11. This timing is rather uniform across the domain most of the year in the observations and is between 1700 and 1900 h (Figs. 11a–d). However, during the summer season, the diurnal peak of rainfall along the Gulf Coast and peninsular Florida occurs between 1900 and 2100 h (Fig. 11c). The RSM–ROMS also shows some similar features although it exhibits more spatial gradient than the corresponding observations (Figs. 11e–h). In the summer, especially, RSM–ROMS shows a diurnal peak over a rage of 1900–2300 h. It is also interesting to note the earlier peak of diurnal precipitation between 1100 and 1500 LT along the west Florida shelf in the summer in RSM–ROMS (Fig. 11g) and similarly along the coasts of Cuba, which is unobserved. However, most climate models display a tendency of showing diurnal precipitation peaks too early over land (Collier and Bowman 2004; Dai 2006; Covey et al. 2016). In fact, Christopoulos and Schneider (2021) find that diurnal precipitation peaks in majority of CMIP6 models ~5.4 h too early over land, which is a marginal improvement over CMIP5 models. In contrast to these studies, our results stand out with diurnal peak of rainfall delayed by 1–4 h. Since the Kain–Fritsch cumulus parameterization scheme used in RSM–ROMS is based on an entraining/detraining plume model that triggers convection at a threshold CAPE, we speculate that this delay in the diurnal rainfall is a result of the delay in reaching the threshold CAPE. This may be a consequence of the 10-km grid resolution of the RSM–ROMS simulation, which however will need to be tested with resolution sensitivity integrations with RSM–ROMS.

d. *Tropical cyclones*

The track density of TCs is shown in Fig. 12 from HURDAT2 and from the RSM–ROMS simulation. The seasonal track density can be viewed as a synthesis of seasonal TC counts, the spatial distribution of TC genesis, and the resulting trajectories of these TCs. Given the mesoscale nature of the TCs, these systems are poorly resolved in the coarsely resolved CESM2 and is therefore not attempted to diagnose them in the CESM2 simulation here. This is besides the fact that a number of fields required to track TCs were not available from the CESM2 simulation.

An automated Lagrangian pointwise tracking algorithm, TempestExtremes (Ullrich and Zarzycki 2017), is employed to identify and track TCs with sustained wind speeds > 13 m s^{-1}, using 6-hourly RSM–ROMS data. This algorithm was successfully used to diagnose TC tracks from RSM–ROMS simulation in Jayasankar et al. (2023). This algorithm involves two steps: (i) identifying suitable candidates at each 6-hourly time step using threshold-based criteria that isolate candidate points within the closed contours and (ii) generating tracks by linking neighboring candidates over time and removing those that do not exhibit consistent behavior. We used the 850-hPa geopotential criteria to identify the systems following Vishnu et al. (2020). According to this criterion, TCs are identified as disturbances where the 850-hPa geopotential advances by 125 m^2 s^{-2} within a 10° radius from the center, accompanied by no less than 82% relative humidity at 850 hPa and a surface geopotential below 800 m^2 s^{-2}, persisting for a minimum of 2 days (i.e., eight 6-hourly time steps). The idea here is not to replicate the individual TC tracks of HURDAT2 in the RSM–ROMS simulation but to realize the gross statistics of the climatological track density of HURDAT2 in the RSM–ROMS simulation.

In Fig. 12, we observe that the RSM–ROMS simulation produces comparable TC track density over the western Atlantic (along the Florida and Carolina Coasts) and over the Caribbean region as HURDAT2. The RSM–ROMS simulation also produces TC tracks along the Gulf Coast of Florida, albeit slightly less than HURDAT2. RSM–ROMS also slightly overestimates the landfalling TCs in the northeastern FA, while it underestimates them along the Gulf Coasts of the FA and over South Florida.

5. Discussion and conclusions

The dynamic downscaling of the regional climate to 10-km grid spacing over the Floridan Aquifer (FA) is demonstrated in this study as a beneficial strategy to overcome the limitations of a coarser resolution (by approximately an order of magnitude) global climate model simulation for the region. The FA is surrounded by relatively warm ocean with a robust surface ocean current that transports critically fresher and warmer water from the tropical Caribbean Sea into the Gulf of Mexico, which is a prime supplier of moisture for majority of weather events in the region. Furthermore, the diurnal variation in precipitation is a critical component of the FA hydroclimate, which influences the land surface processes including evapotranspiration and surface temperature. Many of these aspects are poorly resolved in the global climate models primarily owing to their coarser resolution that does not permit some of these mesoscale features of the regional climate.

In this study, we have downscaled a 30-yr (1985–2014) period of the CESM2 historical run (which is part of the CMIP6) using a regional coupled ocean–atmosphere model (RSM–ROMS). RSM–ROMS features identical grids for both its atmospheric and the oceanic components at 10-km grid spacing centered over the FA. At this 10-km grid spacing, the coastlines and the ocean bathymetry in RSM–ROMS appear more realistic compared to the ~1° grid resolution of CESM2. As stated earlier, the purpose of dynamic downscaling is not to necessarily improve the large-scale features but instead to provide verifiable mesoscale details over the regional domain. This was attempted in this study.

The highlights of this validation over the FA are as follows:

- The seasonal mean precipitation bias appears to be comparable in RSM–ROMS and CESM2 with the former reducing the dry bias in the summer (or wet) season significantly compared to the latter.
- There is a significant improvement in the seasonal mean surface temperature bias both over the land and over the ocean in RSM–ROMS compared to CESM2 over all seasons.
- There is also considerable improvement in the simulation of the Loop Current and its variations in RSM–ROMS relative to CESM2.
- The shape and scale parameters of the gamma distribution fitted to the daily rainfall variability over the JJA season appear to be comparable between the observations and RSM–ROMS, while the CESM2 differs significantly from the observations.
- The diurnal variations in precipitation in RSM–ROMS are comparable to observations.
- There is a reasonable distribution of the climatological TC track density over the domain in the RSM–ROMS simulation compared to HURDAT2.

These highlights suggest that this dynamic downscaling effort could be exploited for useful climate applications in many sectors. Obviously, RSM–ROMS is far from a perfect model. We also show the significant bias of the model especially along the coastal oceans, over the orographic regions of the Appalachian Mountains, and even in some of the mesoscale scale features permitted in the RSM–ROMS simulation. For instance, the variability of the Loop Current in terms of the geostrophic surface eddy kinetic energy is underestimated. Similarly, the terrestrial diurnal amplitude and phase of rainfall across the domain in RSM–ROMS shows gradients that are unsubstantiated in the observations. We are continuously working on these issues to further refine the simulation by conducting ongoing sensitivity studies with the physics of the model, which will be a part of our future work.

Our results in this study show further improvements in comparison with a previous study (Bhardwaj and Misra 2019), which was conducted with a slightly different version of RSM–ROMS and was forced with CCSM4 (a previous generation of CESM2). These improvements are seen in the simulation of the seasonal mean precipitation and SST in both CESM2 and RSM–ROMS of this study compared to CCSM4 and the version of RSM–ROMS used in Bhardwaj and Misra (2019), respectively.

Dynamic downscaling to high spatial and temporal resolution appears to be an immediate solution to meet the needs for climate applications at the regional and local scales. Despite efforts to raise the resolutions of the global climate models from their current operational resolutions, the limitations of the computational resources have limited them to specialized experiments (Hewitt et al. 2020; Haarsma et al. 2020; Moreno-Chamarro et al. 2022). Furthermore, we have seen firsthand that often the data from these global models are not stored at high temporal resolutions even at their coarse horizontal resolution, which is sometimes critical for applications. In such instances, we can customize dynamic downscaling for a limited domain to meet the requirements of the application.

Acknowledgments. We acknowledge the support from NASA Grant 80NSSC22K0595.

Data availability statement. The IMERG rainfall data from NASA were obtained from (IMERG 2024). The ERA5 reanalysis data were from https://www.ecmwf.int/en/forecasts/datasets/reanalysis-datasets/era5, the sea surface height data from AVISO were obtained from https://www.aviso.altimetry.fr/en/home.html, HYCOM ocean reanalysis is available from HYCOM (2024), CPC global surface temperature from CPC (2024), and the observed best track data were from HURDAT2 (2025). The data and the software to generate the figures in the manuscript are available from Misra and Jayasankar (2025).

REFERENCES

Alexander, L. V., M. Bador, R. Roca, S. Contractor, M. G. Donat, and P. L. Nguyen, 2020: Intercomparison of annual precipitation indices and extremes over global land areas from in situ, space-based and reanalysis products. *Environ. Res. Lett.*, **15**, 055002, https://doi.org/10.1088/1748-9326/ab79e2.

Alpert, J. C., M. Kanamitsu, P. M. Caplan, J. G. Sela, G. H. White, and E. Kalnay, 1988: Mountain induced gravity wave drag parameterization in the NMC medium-range forecast model. *Proc. Eighth Conf. on Numerical Weather Prediction*, Baltimore, MD, Amer. Meteor. Soc., 726–733, https://jglobal.jst.go.jp/en/detail?JGLOBAL_ID=200902050067580868.

Bastola, S., and V. Misra, 2013: Sensitivity of hydrological simulations of southeastern United States watersheds to temporal aggregation of rainfall. *J. Hydrometeor.*, **14**, 1334–1344, https://doi.org/10.1175/JHM-D-12-096.1.

Becker, E. J., E. H. Berbery, and R. W. Higgins, 2009: Understanding the characteristics of daily precipitation over the United States using the North American regional reanalysis. *J. Climate*, **22**, 6268–6286, https://doi.org/10.1175/2009JCLI2838.1.

Berner, J., T. Jung, and T. N. Palmer, 2012: Systematic model error: The impact of increased horizontal resolution versus improved stochastic and deterministic parameterizations. *J. Climate*, **25**, 4946–4962, https://doi.org/10.1175/JCLI-D-11-00297.1.

Bhardwaj, A., and V. Misra, 2019: The role of air-sea coupling in the downscaled hydroclimate projection over peninsular Florida and the west Florida shelf. *Climate Dyn.*, **53**, 2931–2947, https://doi.org/10.1007/s00382-019-04669-5.

Bogenschutz, P. A., A. Gettelman, C. Hannay, V. E. Larson, R. B. Neale, C. Craig, and C.-C. Chen, 2018: The path to CAM6: Coupled simulations with CAM5.4 and CAM5.5. *Geosci. Model Dev.*, **11**, 235–255, https://doi.org/10.5194/gmd-11-235-2018.

Capotondi, A., C. Deser, A. S. Phillips, Y. Okumura, and S. M. Larson, 2020: ENSO and Pacific decadal variability in the Community Earth System Model Version 2. *J. Adv. Model. Earth Syst.*, **12**, e2019MS002022, https://doi.org/10.1029/2019MS002022.

Carton, J. A., and B. S. Giese, 2008: A reanalysis of ocean climate using simple ocean data assimilation (SODA). *Mon. Wea. Rev.*, **136**, 2999–3017, https://doi.org/10.1175/2007MWR1978.1.

Chan, S. C., and V. Misra, 2010: A diagnosis of the 1979–2005 extreme rainfall events in the southeastern United States with isentropic moisture tracing. *Mon. Wea. Rev.*, **138**, 1172–1185, https://doi.org/10.1175/2009MWR3083.1.

Charles, S. P., and Coauthors, 2019: Experimental saltwater intrusion drives rapid soil elevation and carbon loss in freshwater and brackish everglades marshes. *Estuaries Coasts*, **42**, 1868–1881, https://doi.org/10.1007/s12237-019-00620-3.

Christopoulos, C., and T. Schneider, 2021: Assessing biases and climate implications of the diurnal precipitation cycle in climate models. *Geophys. Res. Lett.*, **48**, e2021GL093017, https://doi.org/10.1029/2021GL093017.

Chen, J., and X. J. Zhang, 2021: Challenges and potential solutions in statistical downscaling of precipitation. *Climatic Change*, **165**, 63, https://doi.org/10.1007/s10584-021-03083-3.

Chérubin, L. M., W. Sturges, and E. P. Chassignet, 2005: Deep flow variability in the vicinity of the Yucatan straits from a high-resolution numerical simulation. *J. Geophys. Res.*, **110**, C04009, https://doi.org/10.1029/2004JC002280.

Chou, M. D., and M. J. Suarez, 1994: An efficient thermal infrared radiation parameterization for use in general circulation models. NASA Tech. Memo. NASA-TM-104606/Vol. 3, 98 pp., https://ntrs.nasa.gov/archive/nasa/casi.ntrs.nasa.gov/19950009331.pdf.

Chou, M.-D., and K.-T. Lee, 1996: Parameterizations for the absorption of solar radiation by water vapor and ozone. *J. Atmos. Sci.*, **53**, 1203–1208, https://doi.org/10.1175/1520-0469(1996)053<1203:PFTAOS>2.0.CO;2.

Collier, J. C., and K. P. Bowman, 2004: Diurnal cycle of tropical precipitation in a general circulation model. *J. Geophys. Res.*, **109**, D17105, https://doi.org/10.1029/2004JD004818.

Covey, C., P. J. Gleckler, C. Doutriaux, D. N. Williams, A. Dai, J. Fasullo, K. Trenberth, and A. Berg, 2016: Metrics for the diurnal cycle of precipitation: Toward routine benchmarks for climate models. *J. Climate*, **29**, 4461–4471, https://doi.org/10.1175/JCLI-D-15-0664.1.

CPC, 2024: CPC Global Unified Temperature. NOAA, accessed 14 January 2024, https://psl.noaa.gov/data/gridded/data.cpc.globaltemp.html.

Dai, A., 2006: Precipitation characteristics in eighteen coupled climate models. *J. Climate*, **19**, 4605–4630, https://doi.org/10.1175/JCLI3884.1.

——, and K. E. Trenberth, 2004: The diurnal cycle and its depiction in the Community Climate System Model. *J. Climate*, **17**, 930–951, https://doi.org/10.1175/1520-0442(2004)017<0930:TDCAID>2.0.CO;2.

Danabasoglu, G., S. C. Bates, B. P. Briegleb, S. R. Jayne, M. Jochum, W. G. Large, S. Peacock, and S. G. Yeager, 2012: The CCSM4 ocean component. *J. Climate*, **25**, 1361–1389, https://doi.org/10.1175/JCLI-D-11-00091.1.

——, and Coauthors, 2020: The Community Earth System Model Version 2 (CESM2). *J. Adv. Model. Earth Syst.*, **12**, e2019MS001916, https://doi.org/10.1029/2019MS001916.

Danielson, J. J., and D. B. Gesch, 2011: Global multi-resolution terrain elevation data. Open-File Rep. 2011-1073, 23 pp., https://doi.org/10.3133/ofr20111073.

Davies, H. C., 1976: A lateral boundary formulation for multi-level prediction models. *Quart. J. Roy. Meteor. Soc.*, **102**, 405–418, https://doi.org/10.1256/smsqj.43209.

Davies, T., 2014: Lateral boundary conditions for limited area models. *Quart. J. Roy. Meteor. Soc.*, **140**, 185–196, https://doi.org/10.1002/qj.2127.

Dessu, S. B., R. M. Price, T. G. Troller, and J. S. Kominoski, 2018: Effects of sea-level rise and freshwater management on long-term water levels and water quality in the Florida coastal everglades. *J. Environ. Manage.*, **211**, 164–176, https://doi.org/10.1016/j.jenvman.2018.01.025.

Dirmeyer, P. A., and Coauthors, 2012: Simulating the diurnal cycle of rainfall in global climate models: Resolution versus parameterization. *Climate Dyn.*, **39**, 399–418, https://doi.org/10.1007/s00382-011-1127-9.

Ek, M. B., K. E. Mitchell, Y. Lin, E. Rogers, P. Grunmann, V. Koren, G. Gayno, and J. D. Tarpley, 2003: Implementation of Noah land surface model advances in the National Centers for Environmental Prediction operational mesoscale Eta model. *J. Geophys. Res.*, **108**, 8851, https://doi.org/10.1029/2002JD003296.

Eyring, V., S. Bony, G. A. Meehl, C. A. Senior, B. Stevens, R. J. Stouffer, and K. E. Taylor, 2016: Overview of the Coupled Model Intercomparison Project Phase 6 (CMIP6) experimental design and organization. *Geosci. Model Dev.*, **9**, 1937–1958, https://doi.org/10.5194/gmd-9-1937-2016.

Ezer, T., H. Arango, and A. F. Shchepetkin, 2002: Developments in terrain-following ocean models: Intercomparisons of numerical aspects. *Ocean Modell.*, **4**, 249–267, https://doi.org/10.1016/S1463-5003(02)00003-3.

FOCC, 2010: Climate change and sea-level rise in Florida: An update of the effects of climate change on Florida's Ocean and Coastal Resources. FOCC Rep., 36 pp., https://floridadep.gov/sites/default/files/Climate%20Change%20and%20Sea-Level%20Rise%20in%20Florida_1.pdf.

Haarsma, R., and Coauthors, 2020: HighResMIP versions of EC-Earth: EC-Earth3P and EC-Earth3p-HR—Description, model computational performance and basic validation. *Geosci. Model Dev.*, **13**, 3507–3527, https://doi.org/10.5194/gmd-13-3507-2020.

Haidvogel, D. B., H. G. Arango, K. Hedstrom, A. Beckmann, P. Malanotte-Rizzoli, and A. F. Shchepetkin, 2000: Model evaluation experiments in the North Atlantic Basin: Simulations in nonlinear terrain-following coordinates. *Dyn. Atmos. Oceans*, **32**, 239–281, https://doi.org/10.1016/S0377-0265(00)00049-X.

Ham, S., S.-Y. Hong, Y. Noh, S.-I. An, Y.-H. Byun, H.-S. Kang, J. Lee, and W.-T. Kwon, 2012: Effects of freshwater runoff on a tropical Pacific climate in the HadGEM2. *Asia-Pac. J. Atmos. Sci.*, **48**, 457–463, https://doi.org/10.1007/s13143-012-0041-3.

Hersbach, H., and Coauthors, 2019: ERA5 monthly averaged data on pressure levels from 1959 to present. Copernicus Climate Change Service (C3S) Climate Data Store (CDS), https://doi.org/10.24381/cds.6860a573.

Hewitt, H. T., and Coauthors, 2020: Resolving and parameterising the ocean mesoscale in Earth System Models. *Curr. Climate Change Rep.*, **6**, 137–152, https://doi.org/10.1007/s40641-020-00164-w.

Hong, S.-Y., and H.-L. Pan, 1996: Nonlocal boundary layer vertical diffusion in a Medium-Range Forecast Model. *Mon. Wea. Rev.*, **124**, 2322–2339, https://doi.org/10.1175/1520-0493(1996)124<2322:NBLVDI>2.0.CO;2.

Huffman, G. J., and Coauthors, 2023: NASA Global Precipitation Measurement (GPM) Integrated Multi-satellitE Retrievals for GPM (IMERG). Algorithm Theoretical Basis Doc., version 07, 52 pp., https://gpm.nasa.gov/sites/default/files/2023-07/IMERG_V07_ATBD_final_230712.pdf.

——, and Coauthors, 2024: IMERG V07 Release Notes. NASA Tech. Doc., 23 pp., https://gpm.nasa.gov/resources/documents/imerg-v07-release-notes.

Hunke, E. C., W. H. Lipscomb, A. K. Turner, N. Jeffery, and S. Elliott, 2015: CICE: The Los Alamos sea ice model documentation and software user's manual, version 5.1. Doc. LA-CC-06-012, 116 pp.

HURDAT2, 2025: HURDAT2 datasets are available through the NHC Data Archive portal. National Hurricane Center, accessed 20 January 2024, https://www.nhc.noaa.gov/data/.

Hurlburt, H. E., and J. D. Thompson, 1980: A numerical study of loop current intrusions and eddy shedding. *J. Phys. Oceanogr.*, **10**, 1611–1651, https://doi.org/10.1175/1520-0485(1980)010<1611:ANSOLC>2.0.CO;2.

HYCOM, 2024: HYCOM + NCODA global 1/12° analysis. HYCOM, accessed 14 January 2024, https://hycom.org/dataserver/glb-analysis.

IMERG, 2024: Global precipitation measurement. NOAA, accessed 17 January 2024, https://gpm.nasa.gov/data/directory.

Jayasankar, C. B., V. Misra, and N. Karmakar, 2023: A comparative study between regional atmospheric model simulations coupled and uncoupled to a regional ocean model of the Indian summer monsoon. *Earth Space Sci.*, **10**, e2022EA002733, https://doi.org/10.1029/2022EA002733.

Jouanno, J., J. Sheinbaum, B. Barnier, J. M. Molines, and J. Candela, 2012: Seasonal and interannual modulation of the eddy kinetic energy in the Caribbean Sea. *J. Phys. Oceanogr.*, **42**, 2041–2055, https://doi.org/10.1175/JPO-D-12-048.1.

Juang, H.-M., and M. Kanamitsu, 1994: The NMC nested regional spectral model. *Mon. Wea. Rev.*, **122**, 3–26, https://doi.org/10.1175/1520-0493(1994)122<0003:TNNRSM>2.0.CO;2.

Kain, J. S., 2004: The Kain–Fritsch convective parameterization: An update. *J. Appl. Meteor.*, **43**, 170–181, https://doi.org/10.1175/1520-0450(2004)043<0170:TKCPAU>2.0.CO;2.

——, and M. Fritsch, 1993: Convective parameterization for mesoscale models: The Kain-Fritsch scheme. *The Representation of Cumulus Convection in Numerical Models*, *Meteor. Monogr.*, No. 46, Amer. Meteor. Soc., 165–170.

Kanamaru, H., and M. Kanamitsu, 2007: Scale-selective bias correction in a downscaling of global analysis using a regional model. *Mon. Wea. Rev.*, **135**, 334–350, https://doi.org/10.1175/MWR3294.1.

Landsea, C. W., and J. L. Franklin, 2013: Atlantic hurricane database uncertainty and presentation of a new database format. *Mon. Wea. Rev.*, **141**, 3576–3592, https://doi.org/10.1175/MWR-D-12-00254.1.

Lanzante, J. R., K. W. Dixon, M. J. Nath, C. E. Whitlock, and D. Adams-Smith, 2018: Some pitfalls in statistical downscaling of future climate. *Bull. Amer. Meteor. Soc.*, **99**, 791–803, https://doi.org/10.1175/BAMS-D-17-0046.1.

Laprise, R., and Coauthors, 2008: Challenging some tenets of regional climate modelling. *Meteor. Atmos. Phys.*, **100**, 3–22, https://doi.org/10.1007/s00703-008-0292-9.

Large, W. G., J. C. McWilliams, and S. C. Doney, 1994: Oceanic vertical mixing: A review and a model with a nonlocal boundary layer parameterization. *Rev. Geophys.*, **32**, 363–403, https://doi.org/10.1029/94RG01872.

Lawrence, D. M., and Coauthors, 2019: The Community Land Model version 5: Description of new features, benchmarking, and impact of forcing uncertainty. *J. Adv. Model. Earth Syst.*, **11**, 4245–4287, https://doi.org/10.1029/2018MS001583.

Li, H., M. Kanamitsu, and S.-Y. Hong, 2012: California reanalysis downscaling at 10 km using an ocean-atmosphere coupled regional model system. *J. Geophys. Res.*, **117**, D12118, https://doi.org/10.1029/2011JD017372.

——, ——, ——, K. Yoshimura, D. R. Cayan, and V. Misra, 2014: A high-resolution ocean-atmosphere coupled downscaling of the present climate over California. *Climate Dyn.*, **42**, 701–714, https://doi.org/10.1007/s00382-013-1670-7.

Liu, Y., S.-K. Lee, D. B. Enfield, B. A. Muhling, J. T. Lamkin, F. E. Muller-Karger, and M. A. Roffer, 2015: Potential impact of climate change on the Intra-Americas Sea: Part-1. A dynamic downscaling of the CMIP5 model projections. *J. Mar. Syst.*, **148**, 56–69, https://doi.org/10.1016/j.jmarsys.2015.01.007.

Maliva, R. G., W. S. Manahan, and T. M. Missimer, 2021: Climate change and water supply: Governance and adaptation planning in Florida. *Water Policy*, **23**, 521–536, https://doi.org/10.2166/wp.2021.140.

Marella, R. L., 2015: Water Withdrawals in Florida, 2012. U.S. Geological Survey Open-File Rep. 2015-1156, 10 pp., https://pubs.usgs.gov/of/2015/1156/ofr20151156_marella-water-use-2012.pdf.

——, and M. P. Berndt, 2005: Water withdrawals and trends from the Floridan aquifer system in the southeastern United States, 1950-2000. U.S. Geological Survey Circular 1278, 24 pp., https://pubs.er.usgs.gov/publication/cir1278.

——, and J. F. Dixon, 2015: Data tables summarizing the source-specific estimated water withdrawals in Florida by water source, category, county, and water management district. U.S. Geological Survey Data Release 2018-5147, 52 pp.

Maxwell, J. T., P. T. Soulé, J. T. Ortegren, and P. A. Knapp, 2012: Drought-busting tropical cyclones in the southeastern Atlantic United States: 1950–2008. *Ann. Assoc. Amer. Geogr.*, **102**, 259–275, https://doi.org/10.1080/00045608.2011.596377.

McVoy, C., W. P. Said, J. Obeysekera, J. VanArman, and T. Dreschel, 2012: Landscapes and hydrology of the predrainage everglades. *Wetlands*, University Press of Florida, 589–591.

Meehl, G. A., C. Shields, J. M. Arblaster, H. Annamalai, and R. Neale, 2020: Intraseasonal, seasonal, and interannual characteristics of regional monsoon simulations in CESM2. *J. Adv. Model. Earth Syst.*, **12**, e2019MS001962, https://doi.org/10.1029/2019MS001962.

Mellor, G. L., and T. Yamada, 1982: Development of a turbulence closure model for geophysical fluid problems. *Rev. Geophys.*, **20**, 851–875, https://doi.org/10.1029/RG020i004p00851.

Meunier, T., A. Bower, P. Pérez-Brunius, F. Graef, and A. Mahadevan, 2024: The energy decay of warm-core eddies in the Gulf of Mexico. *Geophys. Res. Lett.*, **51**, e2023GL106246, https://doi.org/10.1029/2023GL106246.

Misra, V., and S. M. DiNapoli, 2013: The observed teleconnection between the equatorial Amazon and the Intra-Americas Seas. *Climate Dyn.*, **40**, 2637–2649, https://doi.org/10.1007/s00382-012-1474-1.

——, and A. Mishra, 2016: The oceanic influence on the rainy season of peninsular Florida. *J. Geophys. Res. Atmos.*, **121**, 7691–7709, https://doi.org/10.1002/2016JD024824.

——, and A. Bhardwaj, 2021: Estimating the thermodynamic and dynamic contributions to hydroclimatic change over peninsular Florida. *J. Hydrometeor.*, **22**, 573–586, https://doi.org/10.1175/JHM-D-20-0159.1.

——, and ——, 2022: The impact of air–sea coupling on the simulation of the hydroclimatic change over peninsular Florida. *Climate Dyn.*, **59**, 3763–3779, https://doi.org/10.1007/s00382-022-06294-1.

——, and C. B. Jayasankar, 2025: The value of dynamic downscaling over Floridan Aquifer. https://osf.io/2kbrj/.

——, A. Mishra, and H. Li, 2016: The sensitivity of the regional coupled ocean-atmosphere simulations over the Intra-Americas Seas to the prescribed bathymetry. *Dyn. Atmos. Ocean*, **76**, 29–51, https://doi.org/10.1016/j.dynatmoce.2016.08.007.

——, A. Bhardwaj, and A. Mishra, 2017a: Characterizing the rainy season of peninsular Florida. *Climate Dyn.*, **51**, 2157–2167, https://doi.org/10.1007/s00382-017-4005-2.

——, C. Selman, A. J. Waite, S. Bastola, and A. Mishra, 2017b: Terrestrial and ocean climate of the 20th century. *Florida's Climate: Change, Variations and Impacts*, E. Chassignet et al., Eds., Florida Climate Institute, 485–509, https://doi.org/10.17125/fci2017.ch16.

——, A. Mishra, and A. Bhardwaj, 2018: Simulation of the intraseasonal variations of the Indian summer monsoon in a regional coupled ocean–atmosphere model. *J. Climate*, **31**, 3167–3185, https://doi.org/10.1175/JCLI-D-17-0434.1.

——, ——, and ——, 2019: A coupled ocean-atmosphere downscaled climate projection for the peninsular Florida region. *J. Mar. Syst.*, **194**, 25–40, https://doi.org/10.1016/j.jmarsys.2019.02.010.

Moreno-Chamarro, E., and Coauthors, 2022: Impact of increased resolution on long-standing biases in HighResMIP-PRIMAVERA climate models. *Geosci. Model Dev.*, **15**, 269–289, https://doi.org/10.5194/gmd-15-269-2022.

Muller-Karger, F. E., and Coauthors, 2015: Natural variability of surface oceanographic conditions in the offshore Gulf of Mexico. *Prog. Oceanogr.*, **134**, 54–76, https://doi.org/10.1016/j.pocean.2014.12.007.

NOAA, 2013: National Coastal Population Report: Population Trends from 1970 to 2020. NOAA Tech. Rep., 22 pp., https://cdn.oceanservice.noaa.gov/oceanserviceprod/facts/coastal-population-report.pdf.

NOAA National Geophysical Data Center, 2006: 2-minute Gridded Global Relief Data (ETOPO2)v2. NOAA National Centers for Environmental Information, accessed 10 October 2023, https://doi.org/10.7289/V5J1012Q.

Obeysekera, J., J. Barnes, and M. Nungesser, 2015: Climate sensitivity runs and regional hydrologic modeling for predicting the response of the greater Florida everglades ecosystem to climate change. *Environ. Manage.*, **55**, 749–762, https://doi.org/10.1007/s00267-014-0315-x.

——, W. Graham, M. C. Sukop, A. Tiru, W. Dingbao, G. Kebreab, and M. Benjamin, 2017: Implications of climate change on Florida's water resources. *Florida's Climate: Changes, Variations, and Impacts*, CreateSpace Independent Publishing Platform, 83–124.

Prat, O. P., and B. R. Nelson, 2013: Precipitation contribution of tropical cyclones in the southeastern United States from 1998 to 2009 using TRMM satellite data. *J. Climate*, **26**, 1047–1062, https://doi.org/10.1175/JCLI-D-11-00736.1.

Putrasahan, D. A., I. Kamenkovich, M. L. Hénaff, and B. P. Kirtman, 2017: Importance of ocean mesoscale variability for air-sea interactions in the Gulf of Mexico. *Geophys. Res. Lett.*, **44**, 6352–6362, https://doi.org/10.1002/2017GL072884.

Rahimi, J., and Coauthors, 2024: Future climate projections for South Florida: Improving the accuracy of air temperature and precipitation extremes with a hybrid statistical bias correction technique. *Earth's Future*, **12**, e2024EF004531, https://doi.org/10.1029/2024EF004531.

Randall, D. A., Harshvardhan, and D. A. Dazlich, 1991: Diurnal variability of the hydrologic cycle in a General Circulation Model. *J. Atmos. Sci.*, **48**, 40–62, https://doi.org/10.1175/1520-0469(1991)048<0040:DVOTHC>2.0.CO;2.

Reynolds, R. W., T. M. Smith, C. Liu, D. B. Chelton, K. S. Casey, and M. G. Schlax, 2007: Daily high-resolution-blended analyses for sea surface temperature. *J. Climate*, **20**, 5473–5496, https://doi.org/10.1175/2007JCLI1824.1.

Rickenbach, T. M., R. Nieto-Ferreira, C. Zarzar, and B. Nelson, 2015: A seasonal and diurnal climatology of precipitation organization in the southeastern United States. *Quart. J. Roy. Meteor. Soc.*, **141**, 1938–1956, https://doi.org/10.1002/qj.2500.

Scharffenberg, M. G., and D. Stammer, 2010: Seasonal variations of the large-scale geostrophic flow field and eddy kinetic energy inferred from the TOPEX/Poseidon and Jason-1 tandem mission data. *J. Geophys. Res.*, **115**, C02008, https://doi.org/10.1029/2008JC005242.

Shay, L. K., G. J. Goni, and P. G. Black, 2000: Effects of a warm oceanic feature on Hurricane Opal. *Mon. Wea. Rev.*, **128**, 1366–1383, https://doi.org/10.1175/1520-0493(2000)128<1366:EOAWOF>2.0.CO;2.

Shchepetkin, A. F., and J. C. McWilliams, 2005: The regional oceanic modeling system (ROMS): A split-explicit, free-surface, topography-following-coordinate oceanic model. *Ocean Modell.*, **9**, 347–404, https://doi.org/10.1016/j.ocemod.2004.08.002.

Shi, S., and V. Misra, 2020: The role of extreme rain events in peninsular Florida's seasonal hydroclimate variations. *J. Hydrol.*, **589**, 125182, https://doi.org/10.1016/j.jhydrol.2020.125182.

Simpson, I. R., and Coauthors, 2020: An evaluation of the large-scale atmospheric circulation and its variability in CESM2 and other CMIP models. *J. Geophys. Res. Atmos.*, **125**, e2020JD032835, https://doi.org/10.1029/2020JD032835.

——, and Coauthors, 2023: The CESM2 single-forcing large ensemble and comparison to CESM1: Implications for experimental design. *J. Climate*, **36**, 5687–5711, https://doi.org/10.1175/JCLI-D-22-0666.1.

Smith, R. D., and Coauthors, 2010: The Parallel Ocean Program (POP) reference manual, ocean component of the Community Climate System Model (CCSM). Los Alamos National Laboratory Tech. Rep. LAUR-10-01853, 141 pp., http://www.cesm.ucar.edu/models/cesm1.0/pop2/doc/sci/POPRefManual.pdf.

Spechler, R. M., 1994: Saltwater intrusion and quality of water in the Floridan Aquifer System, northeastern Florida. Water-Resources Investigations Rep. 92-4174, 76 pp., https://pubs.usgs.gov/publication/wri924174.

Srivastava, A., R. Grotjahn, and P. A. Ullrich, 2020: Evaluation of historical CMIP6 model simulations of extreme precipitation over contiguous US regions. *Wea. Climate. Extremes*, **29**, 100268, https://doi.org/10.1016/j.wace.2020.100268.

Srivastava, A. K., R. Grotjahn, P. A. Ullrich, and C. Zarzycki, 2022: Evaluation of precipitation indices in suites of dynamically and statistically downscaled regional climate models over Florida. *Climate Dyn.*, **58**, 1587–1611, https://doi.org/10.1007/s00382-021-05980-w.

Staniforth, A., 1997: Regional modeling: A theoretical discussion. *Meteor. Atmos. Phys.*, **63**, 15–29, https://doi.org/10.1007/BF01025361.

Tan, J., G. J. Huffman, D. T. Bolvin, and E. J. Nelkin, 2019: Diurnal cycle of IMERG V06 precipitation. *Geophys. Res. Lett.*, **46**, 13 584–13 592, https://doi.org/10.1029/2019GL085395.

Tatsumi, Y., 1986: A spectral limited-area model with time-dependent lateral boundary conditions and its application to a multi-level primitive equation model. *J. Meteor. Soc. Japan*, **64**, 637–664, https://doi.org/10.2151/jmsj1965.64.5_637.

Tiedtke, M., 1983: The sensitivity of the time-mean large-scale flow to cumulus convection in the ECMWF model. *Proceedings of ECMWF Workshop on Convection in Large-Scale Models*, ECMWF, 297–316.

Ullrich, P. A., and C. M. Zarzycki, 2017: TempestExtremes: A framework for scale-insensitive pointwise feature tracking on unstructured grids. *Geosci. Model Dev.*, **10**, 1069–1090, https://doi.org/10.5194/gmd-10-1069-2017.

Umlauf, L., and H. Burchard, 2003: A generic length-scale equation for geophysical turbulence models. *J. Mar. Res.*, **61**, 235–265, https://doi.org/10.1357/002224003322005087.

van der Ent, R. J., and H. H. G. Savenije, 2013: Oceanic sources of continental precipitation and the correlation with sea surface temperature. *Water Resour. Res.*, **49**, 3993–4004, https://doi.org/10.1002/wrcr.20296.

Vishnu, S., W. R. Boos, P. A. Ullrich, and T. A. O'Brien, 2020: Assessing historical variability of South Asian monsoon lows and depressions with an optimized tracking algorithm. *J. Geophys. Res. Atmos.*, **125**, e2020JD032977, https://doi.org/10.1029/2020JD032977.

Volosciuk, C., D. Maraun, V. A. Semenov, and W. Park, 2015: Extreme precipitation in an atmosphere general circulation model: Impact of horizontal and vertical model resolutions. *J. Climate*, **28**, 1184–1205, https://doi.org/10.1175/JCLI-D-14-00337.1.

Yang, G.-Y., and J. Slingo, 2001: The diurnal cycle in the tropics. *Mon. Wea. Rev.*, **129**, 784–801, https://doi.org/10.1175/1520-0493(2001)129<0784:TDCITT>2.0.CO;2.

Zhao, Q., and F. H. Carr, 1997: A prognostic cloud scheme for pperational NWP models. *Mon. Wea. Rev.*, **125**, 1931–1953, https://doi.org/10.1175/1520-0493(1997)125<1931:APCSFO>2.0.CO;2.

Wang, C., and D. B. Enfield, 2001: The tropical Western Hemisphere warm pool. *Geophys. Res. Lett.*, **28**, 1635–1638, https://doi.org/10.1029/2000GL011763.

Weisberg, R. H., L. Zheng, and Y. Liu, 2016: West Florida shelf upwelling: Origins and pathways. *J. Geophys. Res. Oceans*, **121**, 5672–5681, https://doi.org/10.1002/2015JC011384.

Wilks, D. S., 2006: *Statistical Methods in the Atmospheric Sciences.* International Geophysics Series, Vol. 100, 2nd ed., Academic Press, 627 pp.

Supplemental Material

Journal of Applied Meteorology and Climatology
The Value of Dynamic Downscaling a CMIP6 Global Climate Model Simulation over the Floridan Aquifer
https://doi.org/10.1175/JAMC-D-25-0037.1

Supplementary Material

The value of dynamic downscaling a CMIP6 global climate model simulation over the Floridan Aquifer

Vasubandhu Misra[1, 2, 3, #] and C. B. Jayasankar[2, 3]

[1]Department of Earth, Ocean and Atmospheric Science, Florida State University, Tallahassee, Florida, U.SA.

[2]Center for Ocean-Atmospheric Prediction Studies, Florida State University, Tallahassee, Florida, U.SA.

Corresponding Author Email: vmisra@fsu.edu

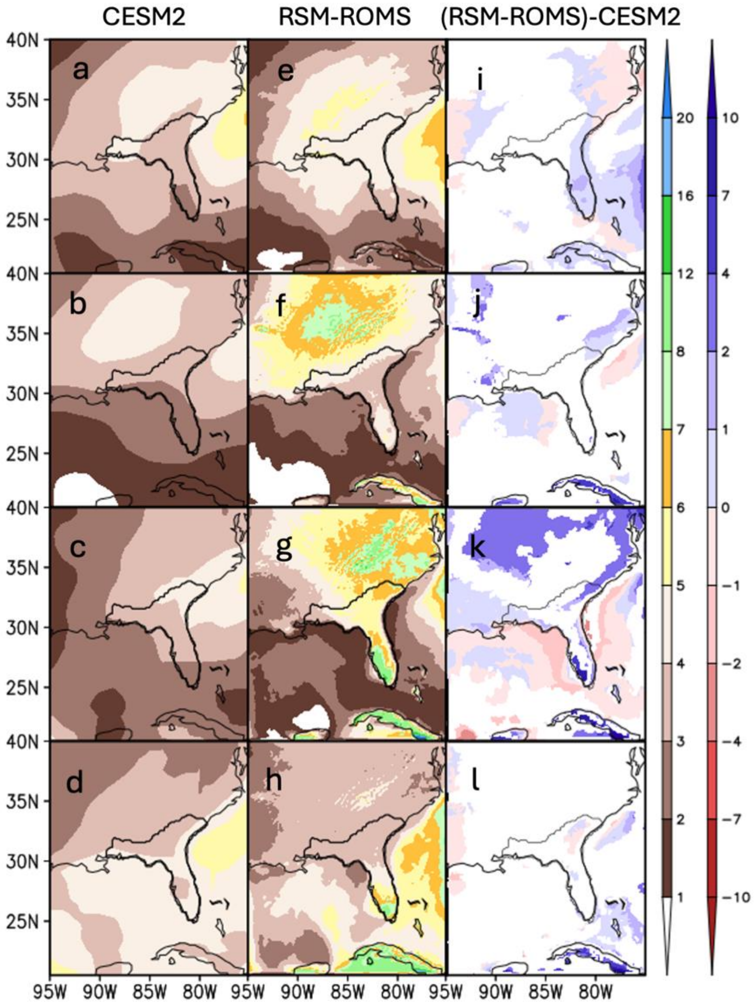

Figure S1: The seasonal climatology of rainfall (mm/day) from (a, b, c, d) CESM2, (e, f, g, h) RSM-ROMS, and (i, j, k, l) (RSM-ROMS)-(CESM2) (mm/day) for (a, e, i) DJF, (b, f, j) MAM, (c, g, k) JJA, and (d, h, l) SON. Only significant values at 5% significance level according to t-test are shaded for the differences. The outline of Floridan Aquifer is overlaid in thick black contour.

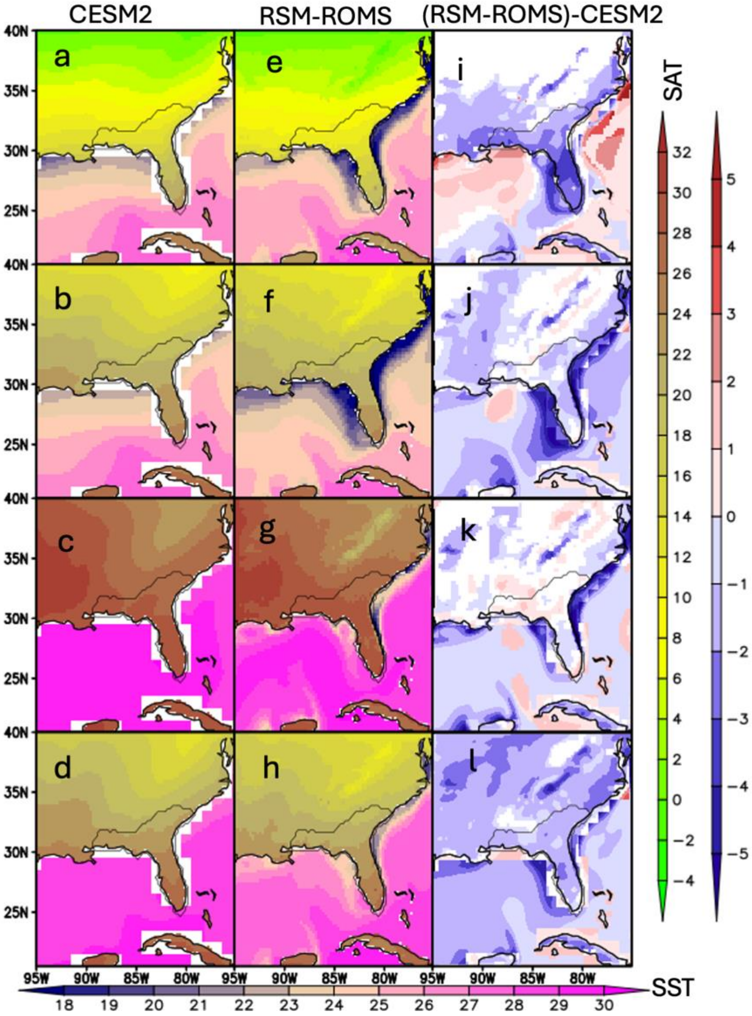

Figure S2: The seasonal climatology of surface temperature (°C) from (a, b, c, d) CESM2, (e, f, g, h) RSM-ROMS, and (i, j, k, l) (RSM-ROMS)-CESM2 for (a, e, i) DJF, (b, f, j) MAM, (c, g, k) JJA, and (d, h, l) SON seasons. Only significant values at 5% significance level according to t-test are shaded for the differences. The outline of Floridan Aquifer is overlaid in thick black contour.

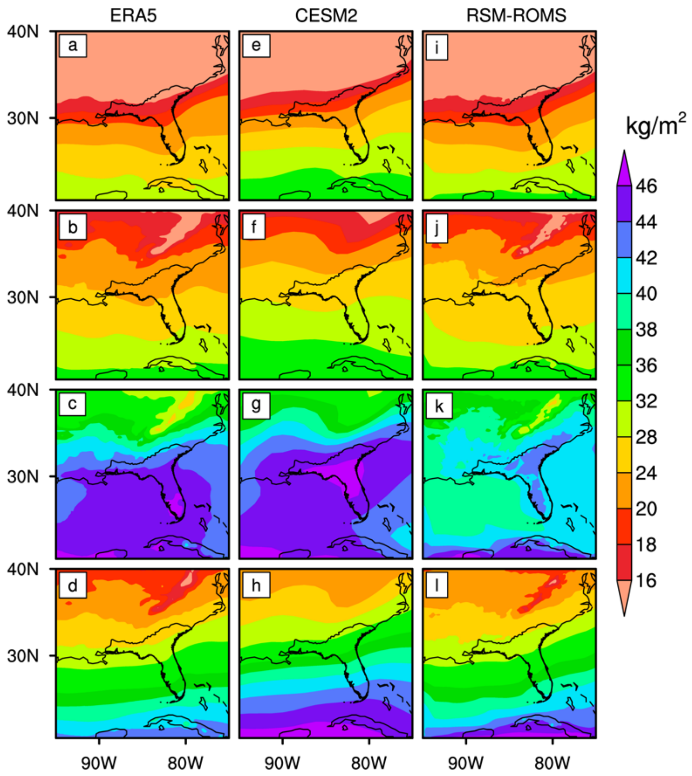

Figure S3: Seasonal climatology of precipitable water (kg/m^2) from (a, b, c, d) observations (ERA5), (e, f, g, h) CESM2, and (i, j, k, l) RSM-ROMS for (a, e, i) DJF, (b, f, j) MAM, (c, g, k) JJA, and (d, h, l) SON seasons. The outline of Floridan Aquifer is overlaid in thick black contour.

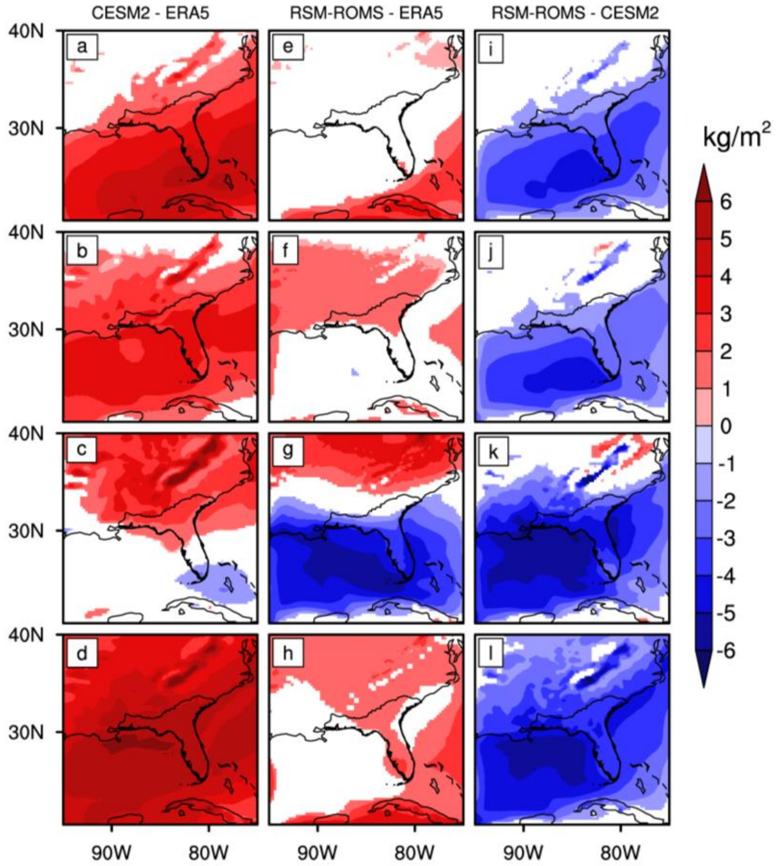

Figure S4: The climatological seasonal bias of precipitable water (kg/m^2) of (a, b, c, d) CESM2 and (e, f, g, h) RSM-ROMS, and (i, j, k, l) (RSM-ROMS)-(CESM2) for (a, e, i) DJF, (b, f, j) MAM, (c, g, k) JJA, and (d, h, l) SON. Only significant values at 5% significance level according to t-test are shaded. The outline of Floridan Aquifer is overlaid in thick black contour.

ST1 Fitting Gamma distribution to daily rainfall

The Gamma distribution PDF, for a given variable y ($\in r$) is given by:

$$f(y) = \frac{(y/\beta)^{\alpha-1} e^{-y/\beta}}{\beta\Gamma(\alpha)}, \qquad y, \alpha, \beta > 0 - - - - - - - - - - - - - -(1)$$

where α is the shape and β is the scale parameters of the distribution. $\Gamma(\alpha)$ is the Gamma function defined by:

$$\Gamma(\alpha) = \int_0^\infty e^{-t}\, t^{\alpha-1} dt - - - - - - - - - - - - - - - -(2)$$

The shape and scale parameters are estimated from the data series using the maximum likelihood estimators following Thom (1958). The estimated $\hat{\alpha}$ and $\hat{\beta}$ are calculated as follows:

$$A = ln(\bar{y}) - \frac{1}{n}\sum_{i=1}^{n} ln(y_n) - (3)$$

$$\hat{\alpha} = \frac{1}{4A}\left(1 + \sqrt{1 + \frac{4A}{3}}\right) - (4)$$

$$\hat{\beta} = \frac{y}{\hat{\alpha}} - - - - - - - - - - - - - -(5)$$

where n is the number of values in y, and A is the sample statistic, which is the difference between the logs of the arithmetic and the geometric means (Wilks 2006). We determine the threshold for a wet day, *t, as* 0.1 mm/day, given that the measurable rain amount at an observation station is typically 0.1 mm (Groisman et al., 1999). The goodness-of-fit is tested using the Chi-square test following Wilks (2006).

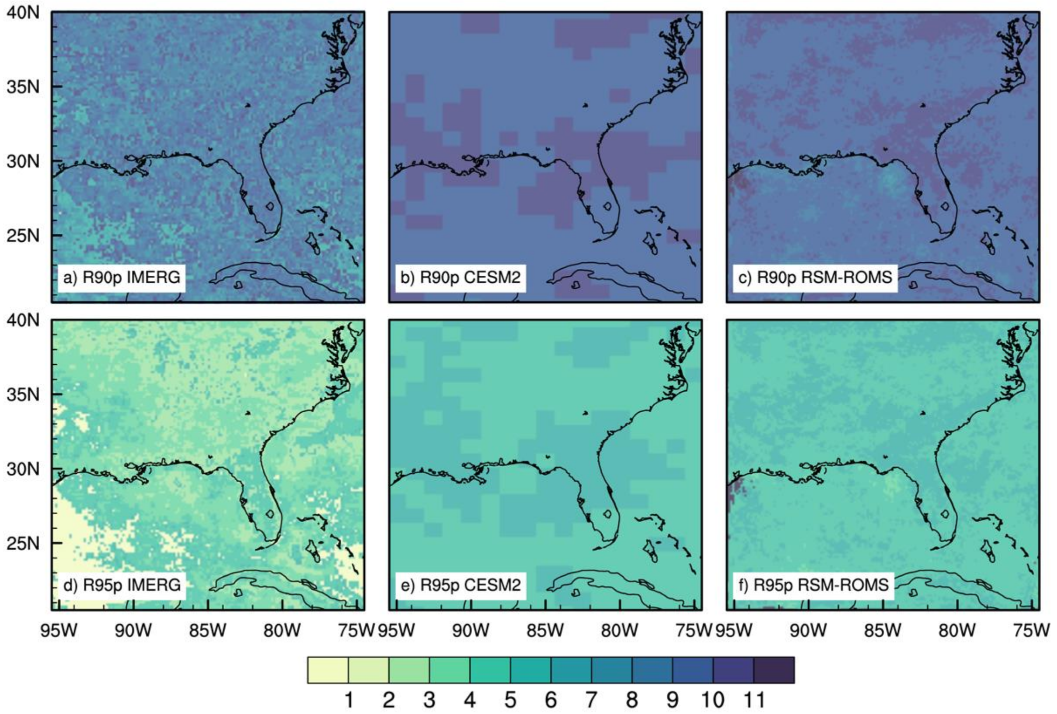

Figure S5: The percentage of number of wet days in JJA when daily precipitation rate exceeds the (a, b, c) 90th (R90p) and (d, e, f) 95th (R95p) percentile thresholds from (a, d) IMERG, (b, e) CESM2, and (c, f) RSM-ROMS simulation.

ST2 Computing seasonal climatology of the surface eddy kinetic energy

We computed the seasonal mean climatology of the surface eddy kinetic energy (K_G) as:

$$K_g = \frac{1}{N}\sum_{i=1}^{N}\bar{k}_{gi} -------------(SE1)$$

Where, i is the year with N being total number of years.

$$\bar{k}_{gJ} = \frac{1}{M}\sum_{j=1}^{M}\left(k_{gj}\right) ------- (SE2)$$

$\bar{k}_{gJ}$ is the seasonal mean surface eddy kinetic energy for season J and M is the total number of months in the season. The surface eddy kinetic energy for the jth month is given as:

$$k_{gj} = \frac{\left[\left(u'_{gj}\right)^2+\left(v'_{gj}\right)^2\right]}{2} ---------- (SE3)$$

Where, $u'_{gj} = \frac{-g}{f}\frac{\partial(ssh')}{\partial y}$ and $v'_{gj} = \frac{g}{f}\frac{\partial(ssh')}{\partial x}$